

School of Science
Department of Physics and Astronomy
Master Degree Programme in Astrophysics and Cosmology

The peculiar nature of Liller 1 from high-resolution CRILES+ spectra

Graduation Thesis

Presented by:
Lanfranco Chiappino

Supervisor:
Chiar.mo Prof. F. R. Ferraro

Co-supervisor:
Dr. C. Fanelli
Dr. L. Origlia
Dr. C. Pallanca

Abstract

General context - The discovery of the complex stellar populations in Terzan 5 and Liller 1, among the most massive stellar systems of the Bulge and more generally of the Galaxy, with a present day mass of a few $10^6 M_{\odot}$, posed new questions about their true nature and their possible connection with the Bulge at the epoch of its formation and early evolution. Indeed, despite their star cluster appearance, the fact that they host sub-populations with significantly different ages (several Gyrs) and metallicities (about 1 dex) indicate that these stellar systems cannot be genuine globulars, which, at variance, are characterized by a single age and metallicity with minor spread, if any. While Terzan 5 has been already photometrically, kinematically and chemically characterized in some detail, Liller 1 still needs a proper chemical investigation.

Scope of the Thesis - The original work presented in this Thesis has concerned the first high-resolution spectroscopic study of the stellar populations in Liller 1, by using high resolution near-IR spectra recently acquired with CRIRES+ at the VLT . Accurate measurements of the chemical abundance of key species as Fe, Mg, Al, Si, S, Ca and Ti, that characterize the environment where Liller 1 formed and the way in which its stellar populations evolved, have been obtained for a first sample of 12 member stars.

Results - The results obtained in this Thesis confirm the photometric existence of at least two major sub-populations with significantly different iron abundance and $[\alpha/\text{Fe}]$ enhancement : a sub-solar component with $[\text{Fe}/\text{H}] \sim -0.3$ and enhanced $[\alpha/\text{Fe}]$, that likely formed at an early epoch from a gas mainly enriched by type II SNe, and a super-solar one with $[\text{Fe}/\text{H}] \sim +0.3$ and about solar-scaled $[\alpha/\text{Fe}]$, that formed at later epochs from a gas also enriched by type Ia SNe. The chemistry of Liller 1 is strikingly similar to the one of Terzan 5 and of the Bulge field. This is the first firm spectroscopic evidence of the complex nature of this stellar system and fully confirms that this is not a genuine globular. The available evolutionary, kinematic and chemical information on Terzan 5 and Liller 1 suggest an in-situ (i.e. bulge) formation and evolution for these systems, thus supporting a scenario where their old stellar sub-populations can be fossil fragments of more massive clumps that may have contributed to form the bulge. These fragments survived total disruption and could evolve and possibly self-enrich as independent systems. The younger sub-populations of Liller 1 and Terzan 5 could be the products of such an evolution.

Structure of the Thesis - This Thesis is structured in five main chapters, that include 1) an introduction with some broad context and the specific scope; 2) the presentation of the spectroscopic database; 3) the description of the spectral analysis; 4) the presentation and discussion of the obtained results; 5) some conclusions and future perspectives. An appendix detailing some of the developed and used software tools and a bibliography are also included.

Contents

1	Introduction	1
1.1	The general problem	2
1.2	Terzan 5 and Liller 1: complex stellar systems in the Galactic bulge . . .	5
1.3	Scope of the Thesis	9
2	The spectroscopic database	11
2.1	The Liller 1 star sample	13
2.2	Observations and data reduction	14
3	Spectral analysis	21
3.1	Continuum normalization, telluric removal and radial velocity correction .	22
3.2	Radial velocity	24
3.3	Effective temperature and surface gravity	25
3.4	Micro- & Macro- turbulence velocities	26
3.5	Chemical analysis	27
4	Results	33
4.1	Line-of-site kinematics	34
4.2	Stellar parameters	35
4.3	Chemical abundances	38
5	Conclusions and future perspectives	43
A	Software Tools	47
A.1	Tools for chemical analysis	48
A.2	Tools for the treatment of observed spectra	53
A.3	Tools to test spectral synthesis	56

Chapter *1*

Introduction

This chapter presents the general context and astrophysical problem as well as the specific scope of this Thesis work, that has concerned the investigation of the chemical properties of Liller 1, a massive, complex stellar system in the Galactic bulge.

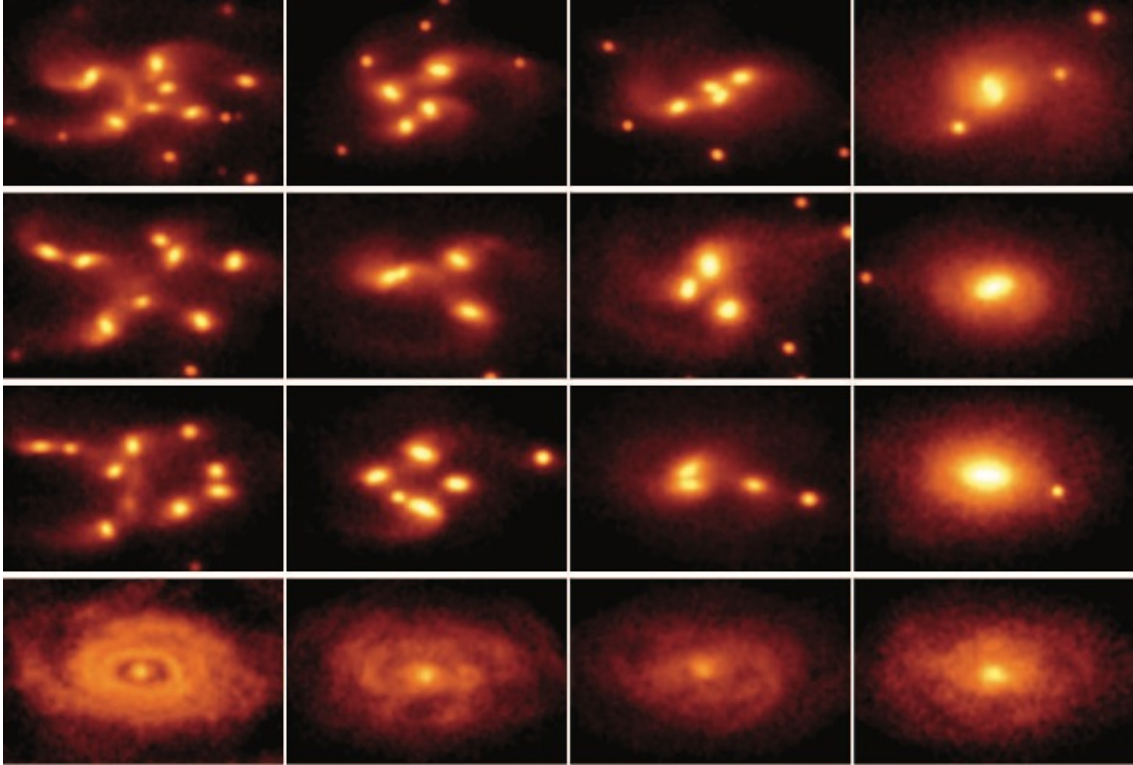


Figure 1.1: High-resolution models without (top row) and with supernova feedback, the feedback efficiency increasing from the second row to the bottom row. The color codes the mass density in log scale, each panel covers an area of $14 \times 8 \text{ kpc}^2$. From left to right, time increases: $t=200 \text{ Myr}$, $t=375 \text{ Myr}$, $t=500 \text{ Myr}$, $t=750 \text{ Myr}$.

1.1 The general problem

The formation of galaxy bulges is a highly debated topic in the literature, with a number of scenarios and mechanisms proposed to explain their origins. The Λ CDM cosmological model describes well how cosmic structures are formed through merging mechanisms, and the bulges of spiral galaxies are not excluded.

They may in fact form through the coalescence of primordial clumps at the time of the galaxy formation. Extensive numerical simulations (Bournaud and Elmegreen, 2009; Elmegreen et al., 2008; Immeli et al., 2004) and high-redshift observations of "clumpy" or "chain galaxies" (Elmegreen et al., 2009; Genzel et al., 2011; Tacchella et al., 2015) have provided important clues about the possible formation of bulges and more generally of stellar spheroids, via coalescence of primordial sub-structures.

According to these studies, at the time of the galaxy formation, gas-rich primordial discs fragment into clumps due to gravitational instabilities. These clumps can grow and ignite star formation within them, leading to the formation of chain and/or clumpy galaxies.

The stars form fast enough to become enriched with iron and α -elements, leaving a chemical signature. Over time, the formed density waves can drive material, including the young clumps, toward the center of the galaxy, leading to a build-up of mass in the central region.

Further evolution foresees clump coalescence and the formation of massive, disk galaxies, as observed today.

Fig. 1.1 shows a simulation which describes how these massive clumps, generated through violent disk instabilities, have the potential to migrate towards the center of the galaxy and coalesce, contributing to the growth of the bulge (Elmegreen et al., 2008) and whether energy injected by SNe can disrupt the clumps before they reach the center.

The first row shows a model that includes star formation but no SN feedback, with an initial gas fraction of 60%, an initial bulge of 4% of the disk. From the second to the bottom row, models have the same initial conditions and resolution as the first one, but with supernova feedback included. In particular they have different fractions ϵ of the 10^{51} erg energy of each supernova re-injected into the local gas kinetic energy, namely $\epsilon = 2 \times 10^{-4}$, $\epsilon = 2 \times 10^{-3}$, $\epsilon = 2 \times 10^{-2}$, respectively. By increasing the feedback efficiency, clumps become shorter-lived and rapidly disrupted.

Models also suggest that the most massive clumps can survive total disruption from star formation feedbacks, thus occasionally evolving as independent sub-structures and appearing as massive globulars in the innermost regions of their host galaxies (Bournaud, 2016).

From the observational side, galaxies with $z > 1$ exhibit growing levels of clumpiness and irregularity, due to the increasing star formation rate and interactions in the early Universe. Fig. 1.2 shows examples of chain, clumpy and spiral galaxies (Elmegreen et al., 2009). These structures are dominated by giant star-forming regions. By measuring magnitudes and colors and using population synthesis models some information on the clump masses, ages and star formation rate can be obtained. Approximately 30% of the chain galaxies and 50% of the clumpy galaxies contain bright red clumps with 10^8 - $10^9 M_{\odot}$, that could coalesce and form massive bulges/bars/disks in the central regions of their host.

The Milky Way Bulge, because of its vicinity, offers a unique opportunity to perform a comprehensive evolutionary, kinematic and chemical study of its resolved stellar populations and to find possible signatures of its formation and early evolution, e.g. in the form of fossil fragments, with a major impact in our overall understanding of galaxy bulges in general.

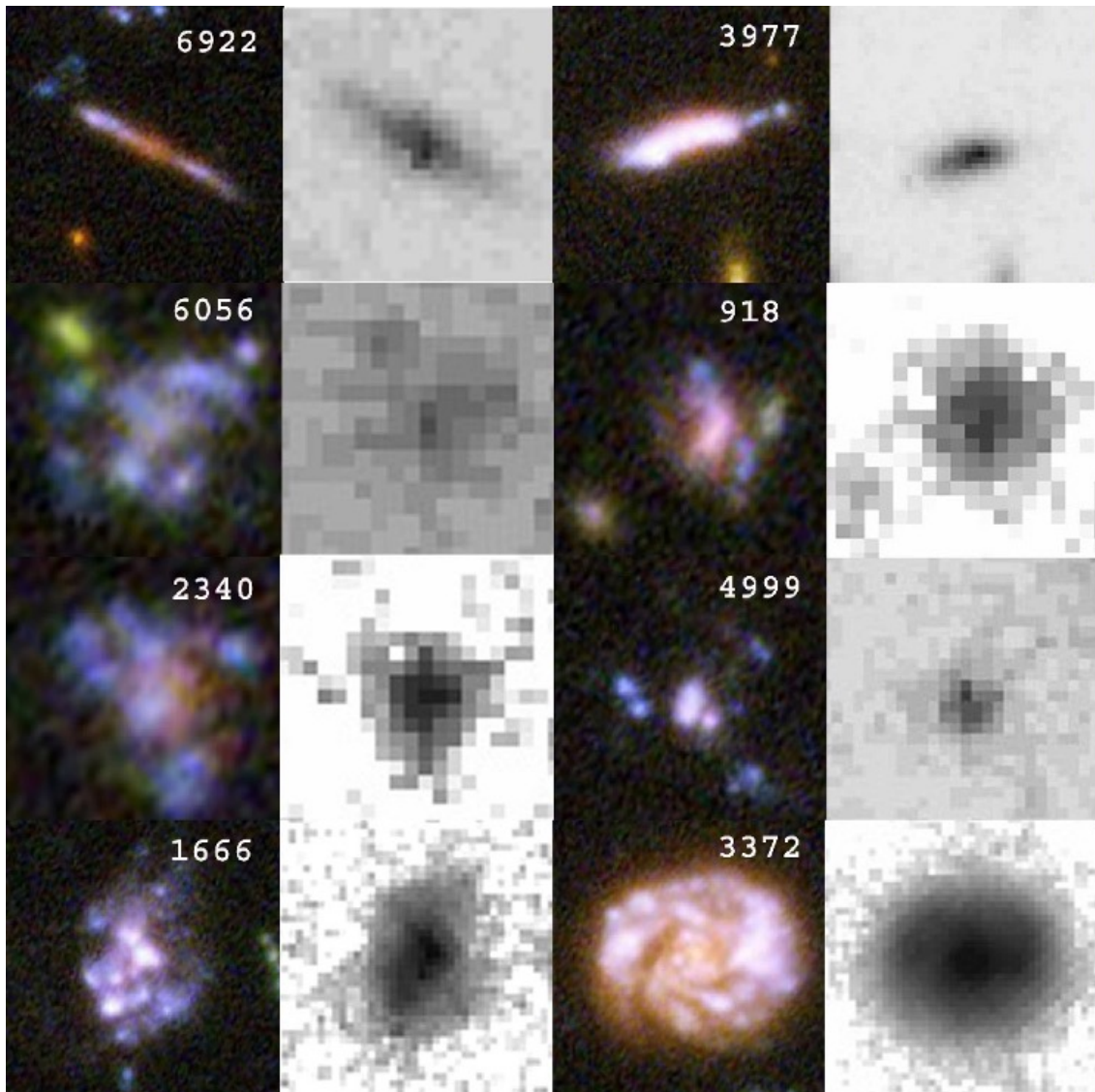


Figure 1.2: ACS (color) and NICMOS H-band (grey) images for eight representative galaxies (from Elmegreen et al., 2009).

1.2 Terzan 5 and Liller 1: complex stellar systems in the Galactic bulge

Terzan 5 and Liller 1 are massive and very reddened stellar systems of the Galactic Bulge, traditionally classified as globular clusters. However, a detailed photometric investigation of Terzan 5 (Ferraro et al., 2009, 2016) and Liller 1 (Ferraro et al., 2021) stellar populations has revealed the presence of multiple sub-populations with significantly different ages and metallicities, thus unveiling a much more complex nature and triggering new questions about their origin and evolution.

Terzan 5 is located at 5.9 kpc from the Galactic center, and it has an average $E(B-V)$ of ~ 2.5 mag and a differential reddening, whose range spans ~ 0.7 mag (Massari et al., 2012). Terzan 5 hosts at least two main sub-populations, one about 12 Gyr old with sub-solar metallicities with a peak at $[Fe/H] \approx -0.3$ dex and a possible second peak/tail at $[Fe/H] \approx -0.8$ dex, and a younger sub-population with an age of ~ 4.5 Gyr (see Fig. 1.3) and with super-solar metallicity peaking at $[Fe/H] \approx +0.3$ dex (Ferraro et al., 2016; Massari et al., 2014).

HST proper motions (PMs) measurements also shows that the metal-rich component is more centrally concentrated than the metal-poor one (Ferraro et al., 2009; Massari et al., 2015).

Subsequent spectroscopic investigations of the detailed chemistry of a representative sample of Terzan 5 member giants and variables stars (Origlia et al., 2011, 2013) also revealed that the old sub-populations are α -enhanced, having formed from a gas mainly enriched by type II SNe on a short time-scale at early epochs, while the young sub-population has about solar-scaled $[\alpha/Fe]$ abundance ratios, indicating that these stars formed from a gas also enriched by type Ia SNe on a longer time-scale. Indeed, type II SNe produce large amounts of alpha elements exploding at the end of the short life (10-100 Myr) of massive stars, while type I SNe are large producers of Fe and Fe-group elements, and explode after ~ 1 Gyr from the on-set of the star formation event.

Fig. 1.3 shows the Terzan 5 $K_s(I-K_s)$ CMD with highlighted the old and young Turn-off regions, its metallicity distribution with three peaks and the corresponding $[\alpha/Fe]$ abundance ratio as a function of the iron abundance. Both the metallicity and the $[\alpha/Fe]$ distributions of Terzan 5 closely resemble those of the Bulge, pointing towards a strong chemical link between the two stellar systems.

Terzan 5 radial velocities and PMs from HST (Massari et al., 2015) and more recently from Gaia (Baumgardt et al., 2019; Massari et al., 2019) allowed to determine its orbital parameters with an apocenter of 2.8 kpc, confining it within the bulge and supporting the chemical evidence of an in-situ formation and evolution.

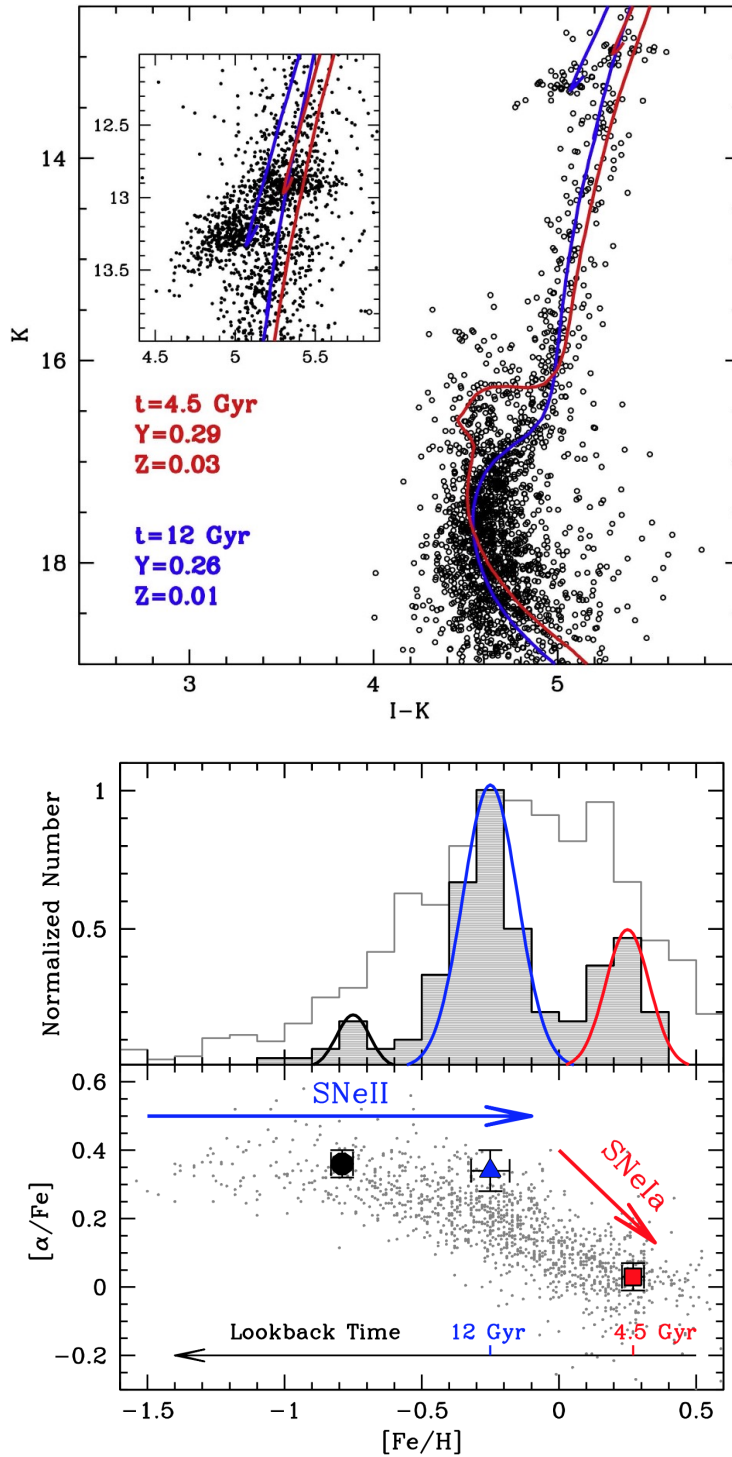


Figure 1.3: Top panel: differential reddening corrected CMD of Terzan 5 obtained by combining the deepest VLT-MAD K-band and HST-ACS I-band images. The blue line traces the 12 Gyr old isochrone of the metal-poor population; the red line traces the younger 4.5 Gyr isochrone of the metal-rich population. The inset shows a zoom of the Red Clump region. Bottom panels: iron distribution of the three sub-populations of Terzan 5 (shaded histogram and colored lines) compared to that of the Galactic bulge field stars from the literature (light gray histogram on the background); $[\alpha/\text{Fe}]-[\text{Fe}/\text{H}]$ distribution of the three sub-populations of Terzan 5 compared to that of the bulge field stars from the literature (gray dots).

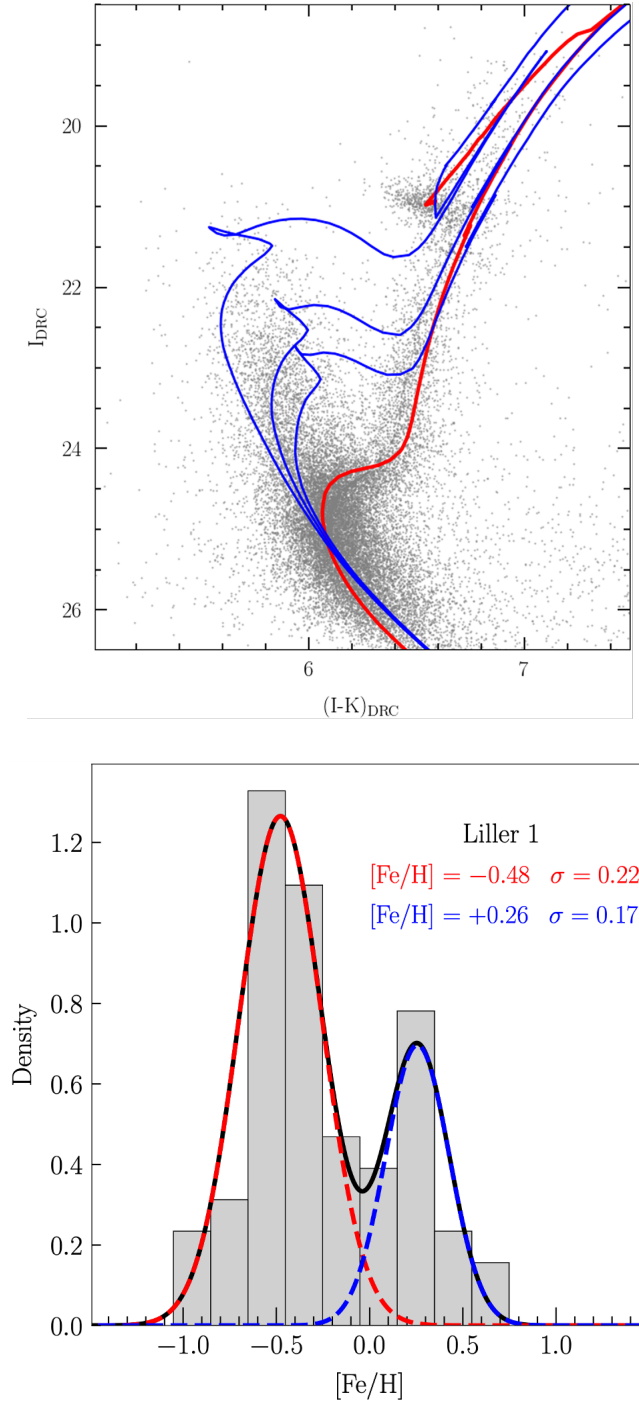


Figure 1.4: Top panel: Differential reddening-corrected and PM-selected I,(I-K) CMD of Liller 1 (gray dots) with isochrones of different age and metallicity overplotted: in red the 12 Gyr old isochrone with metallicity of -0.3 dex, to match the main old sub-population with sub-solar metallicity; in blue three young isochrones (of 1, 2, and 3 Gyr, from top to bottom) at a super-solar metallicity of +0.3 dex, to reproduce the young sub-populations (from Dalessandro et al., 2022; Ferraro et al., 2021). Bottom panel: Metallicity distribution of Liller 1 member stars (grey histogram). The solid black line shows the function that best reproduces the observed distribution. It is the combination of two Gaussian functions for the metal-poor (red line) and metal-rich (blue line) sub-populations, respectively. The corresponding mean $[\text{Fe}/\text{H}]$ values and their standard deviations are also reported (from Crociati et al., 2023).

Liller 1 is located at 0.8 kpc from the Galactic center and it has an even larger reddening than the one in Terzan 5, with an average $E(B-V)$ of ~ 4.5 mag and differential reddening $\delta E(B-V)$ between -0.57 and 0.37 mag (Pallanca et al., 2021), thus remaining relatively unexplored until very recently.

A high quality, deep color-magnitude diagram (CMD) from a combination of HST and GSAOI images in the I and K bands (Ferraro et al., 2021) has revealed the presence of multiple sub-populations within Liller 1 as well, differing significantly in age and metallicity: a main 12 Gyr old population with sub-solar metallicity and younger (1-3 Gyr old, only), metal-rich sub-populations.

So far, the only chemical abundances from high resolution spectra comes from the IR spectroscopic study of two individual giant stars belonging to Liller 1 old and metal-poor population, by using the NIRSPEC spectrograph at Keck II (Origlia et al., 2002), with $[Fe/H] = -0.3 \pm 0.2$ dex, and $[\alpha/Fe]$ enhancement.

Recently, the first Liller 1 metallicity distribution has been derived from low resolution VLT-MUSE spectra (Crociani et al., 2023) in the Ca triplet region, finding that both the metal-poor component with a peak at $[Fe/H] \approx -0.5$ dex and the metal-rich one with a peak at $[Fe/H] \approx +0.3$ dex have quite broad distributions, with a 1σ dispersion of about 0.2 dex.

Fig. 1.4 shows the differential reddening-corrected and PM-selected I,(I-K) CMD (Dalessandro et al., 2022; Ferraro et al., 2021) of Liller 1 with isochrones of different age and metallicity overlaid: a 12 Gyr old isochrone with metallicity of -0.3 dex to match the main old sub-population with sub-solar metallicities and three young isochrones of 1, 2, and 3 Gyr, at a super-solar metallicity of $+0.3$ dex, to reproduce the young sub-populations. It also shows the metallicity distribution (Crociani et al., 2023) of Liller 1 member stars, with highlighted the sub-solar and super-solar broad sub-components.

Such a high-quality CMD has been also used as reference for the modeling of the Liller 1 star formation history (SFH) (Dalessandro et al., 2022).

The best-fit solution reveals that Liller 1 has been actively engaged in star formation for nearly its entire existence, characterized by the presence of three distinct star formation episodes. The main episode started approximately 12-13 Gyr ago, with a tail extending for about 3 Gyr. This initial star formation event is responsible for approximately $\sim 70\%$ of the system current total mass.

The second peak in star formation occurred between 6 and 9 Gyr ago, contributing an additional approximately $\sim 15\%$ to the system mass. The most recent star formation event started around 3 Gyr ago and ceased ~ 1 Gyr ago, when a quiescent phase begun. The analysis reveals that the young population constitutes at least $\sim 10\%$ of Liller 1 total mass.

A detailed chemical analysis of a representative sample of Liller 1 stars based on high resolution spectroscopy, as already done for Terzan 5 (Origlia et al., 2013, and references therein), is definitely urgent, in order to constrain chemical enrichment scenarios and timescales.

1.3 Scope of the Thesis

The complex age and metallicity distributions of Terzan 5 and Liller 1 have unveiled their complex nature, hosting sub-populations with significantly different iron abundances and formed through different star formation episodes over several Gyrs.

A detailed chemical characterization of the content of fundamental species such as iron, α -elements and a few other metals in Liller 1 has become recently possible thanks to the availability of K-band echelle spectra of a representative sample of Liller 1 giant stars.

The first chemical study of the detailed chemistry of Liller 1 has been the objective of this Thesis work. To this purpose, original tools have been developed for data reduction and spectral analysis, including spectrum rectification and normalization, telluric and radial velocity correction, measurement of stellar parameters and chemical abundances.

Chapter 2 reports the properties of the selected sample of Liller 1 stars and a description of the observations and data reduction procedures. Spectral and chemical analysis techniques are described in Chapter 3, while results are detailed in Chapter 4. An astrophysical discussion of the obtained results and future perspectives are briefly reported in Chapter 5, while the Appendix A reports some additional information on the developed and used software tools.

Chapter 2

The spectroscopic database

The 21000-23500 Å spectral range within the K-band is particularly suitable to study the chemistry of heavily reddened stars, since it contains numerous atomic and molecular transitions of iron and α elements (Mg, Si, S, Ca, Ti), which are well measurable in cool giants and powerful tracers of the formation, evolution, and enrichment timescales of those stellar populations. Furthermore, the K band is also rich in CO, OH, CN and HF molecular lines that can be measured at high spectral resolution and from which accurate abundances of carbon, oxygen, nitrogen and fluorine can be derived. These elements provide crucial insights into the physical conditions and chemical mixing processes of cool stellar atmospheres in the Post Main Sequence evolutionary phases.

It is interesting to mention that in the K-band dust extinction is about ten times lower than in the visual. Hence, in the case of Liller 1, extinction is about 14 mag in the V-band, 4.0 mag in the J-band, 2.5 mag in the H-band and 1.6 mag in the K-band. High resolution spectroscopy in the K band is thus optimal for studying the chemistry of Liller 1.

However, only in the last two decades, efficient, medium-high resolution spectrographs working in the NIR spectral range start to become available for quantitative spectroscopy, and a comprehensive definition of optimal linelists, stellar parameter and chemical diagnostics, model atmospheres etc. is still work in progress within the international Community.

The chemical studies of cool star atmospheres in the K band are still mostly sparse, indicating that the astrophysical potential of this spectral region has still to be fully exploited.

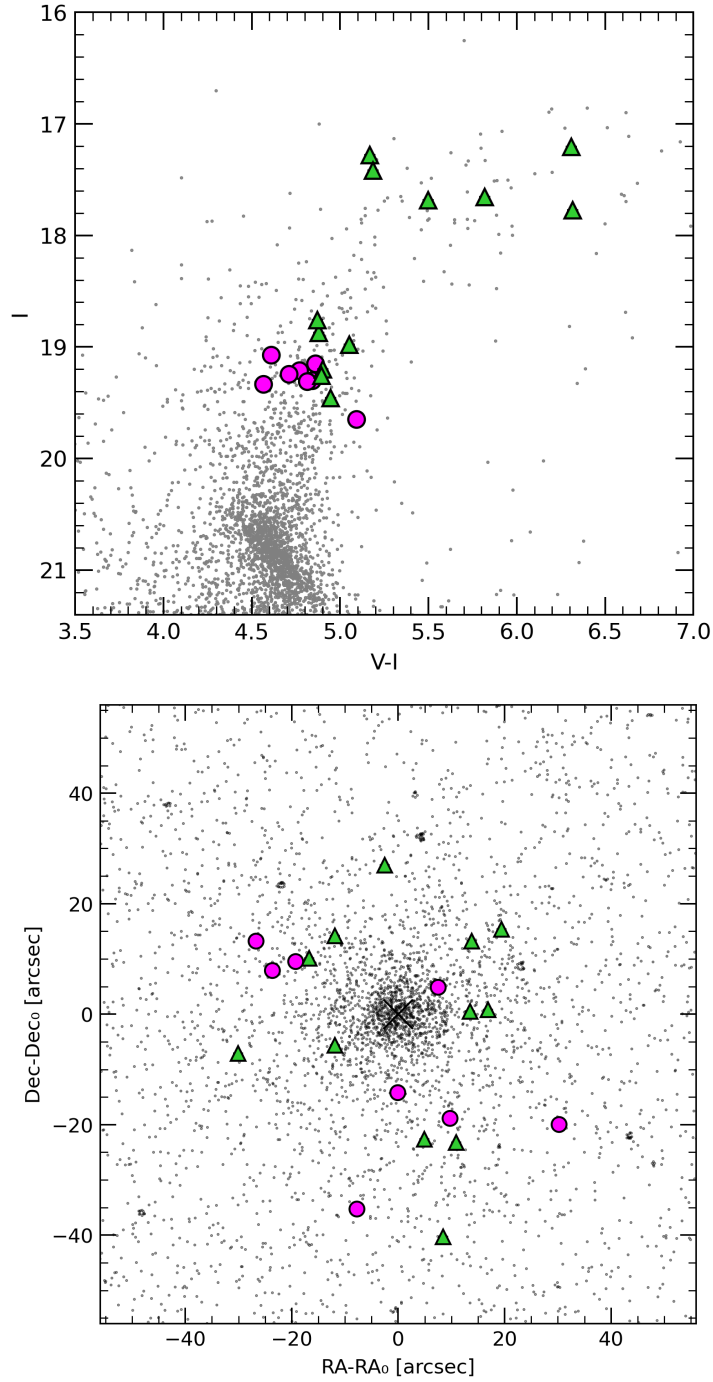


Figure 2.1: $I,(V-I)$ CMD corrected for differential reddening (top panel) and RA-Dec map (bottom panel) of Liller 1 stars, with highlighted those observed with CRIRES+: in green the 12 stars already analysed in this Thesis work, in magenta the remaining 8 stars. The values of RA and Dec are relative to the cluster centre $\text{RA}_0=263.3523333$, $\text{Dec}_0=-33.3895556$ coordinates.

Table 2.1: Analysed target stars in Liller 1.

ID	RA (deg)	Dec (deg)	V	I	K	$\delta E(B-V)$	obs date	T_{exp} (sec)
400087	263.3561440	-33.3858760	23.51	17.21	9.28	0.011	16/04/2023	30×2
300097	263.3491370	-33.3856470	22.44	17.28	10.13	-0.099	16/04/2023	45×2
200119	263.3439575	-33.3915306	22.60	17.42	10.38	-0.246	24/07/2022	45×2
100157	263.3537148	-33.3957827	23.47	17.67	10.01	0.058	16/04/2023	30×2
300162	263.3478150	-33.3866650	23.18	17.68	10.49	-0.147	31/07/2022	45×2
200179	263.3490171	-33.3911168	24.09	17.77	10.01	-0.113	24/07/2022	45×2
400476	263.3516267	-33.3820491	23.63	18.76	11.77	-0.062	13/05/2023	240×2
400519	263.3577128	-33.3852708	23.75	18.87	11.67	0.024	12/05/2023	240×2
100689	263.3553501	-33.3959916	24.10	19.20	12.13	-0.027	13/05/2023	300×2
400733	263.3560726	-33.3894022	24.15	19.26	12.31	0.038	13/05/2023	300×2
400860	263.3570144	-33.3893289	24.40	19.46	12.10	0.121	13/05/2023	300×2
100571	263.3546688	-33.4007517	24.03	18.98	11.75	-0.101	12/05/2023	240×2

Note: The exposure time is the total integration in each AB nodding cycle.

2.1 The Liller 1 star sample

A comprehensive sample of 20 evolved stars of Liller 1, sufficiently bright to be observed at high spectral resolution in the K-band with CRIFES+, has been selected from the HST I,(V-I) CMD (Ferraro et al., 2021), corrected for differential reddening (see Fig. 2.1, top panel). The selected stars have I-band magnitudes in the 17-20 magnitude range. All these stars are located within the central arcmin in radius from the cluster center (see Fig. 2.1, bottom panel).

For these stars some information on their radial velocities and metallicities were already available from low resolution spectra, thus maximizing the probability of selecting member stars, representative of the two main sub-populations of Liller 1, for observations with CRIFES+.

In the present thesis work a detailed chemical analysis of iron and alpha elements has been performed on the 12 brightest stars in the sample, with K-band magnitudes between 9 and 12.

Table 2.1 lists coordinates, magnitudes corrected for differential reddening, observing dates, differential reddening and exposure times for these analyzed targets.



Figure 2.2: CRiRES+ spectrograph at one Nasmyth focal station of the VLT.

2.2 Observations and data reduction

The spectroscopic observations have been carried out under program 109.230K (PI: F. Ferraro) granted 20hr of observing time with CRiRES+ (CRyogenic IR Echelle Spectrograph) at the Very Large Telescope (VLT).

CRiRES+* is a state-of-the-art cross-dispersed echelle spectrograph mounted at one of the Nasmyth focal station of the VLT (see Fig. 2.2), with exceptional capabilities in high-resolution IR spectroscopy with simultaneous large spectral coverage in a single observation.

An echelle spectrograph is a type of spectrograph specifically optimized for high-resolution spectroscopy. It operates by employing a diffraction grating that disperses light into a series of closely spaced, overlapping spectral orders, that are then cross-dispersed along the Y-axis of the detector. This design allows for a large range of wavelengths to be simultaneously recorded on the detector, providing detailed spectral information with exceptional resolving power.

*http://www.eso.org/sci/facilities/paranal/instruments/crises/doc/ESO-323064_2_CRiRES+UserManual.pdf

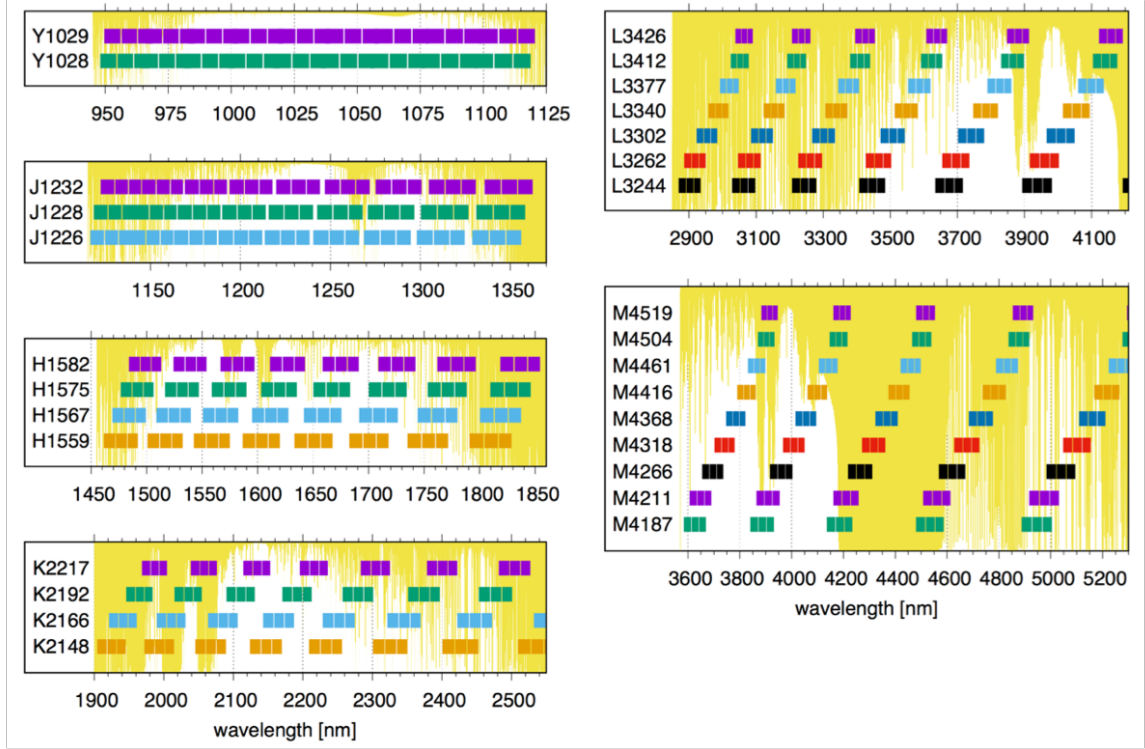


Figure 2.3: CRiRES+ spectral coverages for the various grating configurations in the NIR Y,J,H,K bands and in the mid-IT L,M bands.

CRiRES+ can observe in the NIR (Y,J,H,K bands) and mid-IR (L,M bands) spectral range from 9500 up to 53000 Å at a resolving power of $R=100,000$ with a 0.2 arcsec slit and at $R=50,000$ with a 0.4 arcsec slit. The slit length projected on sky is 10 arcsec.

CRiRES+ uses 3 detectors of $2k \times 2k$ pixels each, thus having about 6000 pixels along the dispersion direction (X-axis on the detector) and 2000 pixels along the cross-dispersion direction (Y-axis on the detector).

By varying the echelle angle and the cross-disperser grating, CRiRES+ is able to fully cover each Y,J,H,K,L,M photometric band (see Fig. 2.3) with a small number of configurations, depending on the particular band.

Two settings are required to fully cover the shorter wavelength region, i.e the Y band, while three settings are needed to fully cover the J band and four settings to cover the H and K bands. Several settings are needed to fully cover the mid-IR L and M bands.

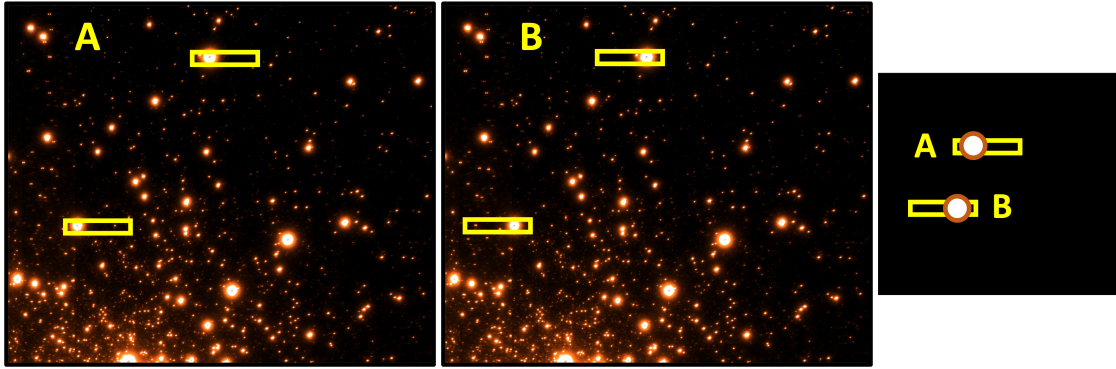


Figure 2.4: A (left panel) and B (middle panel) positioning of two target stars of Liller 1 along the CRIRES+ 10 arcsec slit.

The conventional procedure employed in IR spectroscopy is to observe a designated target at two distinct positions along the slit (named A and B), a practice commonly referred to as "nodding on slit".

The target is alternatively centered on position A and B along the slit. The separation between the "A" and "B" positions, named "nodding throw", has to be set by the observer in order to avoid contamination by nearby stars, but it cannot exceed the slit length of 10 arcsec. Typically, for the observations of the Liller 1 stars, nodding throws between 4 and 6 arcsec have been selected.

This technique is specifically adopted to optimally subtract the background and other instrument effects.

Fig. 2.4 shows the A and B positioning of two Liller 1 targets along the 10 arcsec slit, while Fig. 2.5 shows the corresponding 2D spectra in the K2166 configuration, together with the pair of (A-B) and (B-A) spectra, that is a pair of target-sky spectra.

The total on-source integration time is given by the sum of the N A,B pairs of sub-exposures, where N is the requested number of AB nodding cycles.

Observations of the Liller 1 stars have been performed using the 0.4 arcsec slit at $R=50,000$, the K2166 spectral setting and 1 AB nodding cycle for a total on-source integration time varying from 1 to 10 minutes (see Table 2.1), depending on the target brightness, providing an average signal-to-noise ratio ≥ 50 .

The 2D raw spectra have been processed through the CRIRES+ data reduction pipeline and a few additional tools to optimize spectrum extraction in crowded fields, in order to obtain 1D, background subtracted, flat-field corrected and wavelength calibrated spectra.

When using ground-based telescopes, the light passes through Earth's atmosphere before being collected by the instruments and it efficiently interacts with the molecules there, producing significant absorptions, especially in the infrared region of the spectrum, where many transitions mostly due H_2O , O_2 , CO_2 , CH_4 molecules are observed.

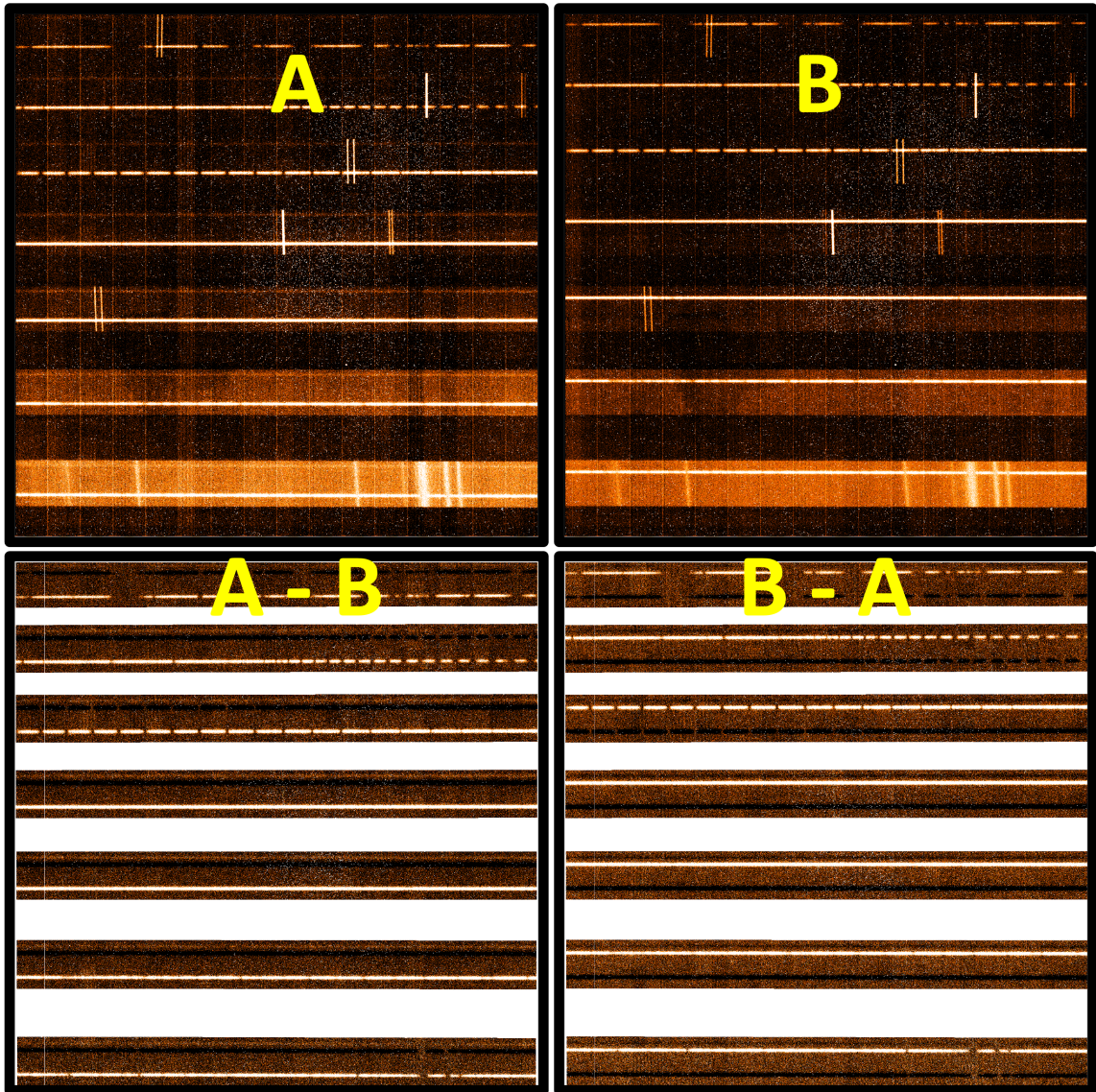


Figure 2.5: CRIFRES+ 2D spectra in the K2166 configuration of a Liller 1 star. Top panels: A and B spectra with the star positioned at the bottom and at the top of the slit, respectively. The brightest OH sky emission lines are visible as well as the thermal emission in the bottom orders at wavelength > 2.3 micron. Bottom panels: A-B and B-A computed spectra for optimal background and sky line subtraction.

Astronomers refer to this process as telluric absorption.

For this work, synthetic telluric spectra generated by means of the TAPAS portal[†] are used to remove telluric absorption from the target spectra. Within the TAPAS portal, the proper observing date (see table 2.1) and site (i.e. Paranal in Chile) must be specified in order to realistically model the telluric absorption during the observation of the target stars.

[†]<https://tapas.aeris-data.fr/>

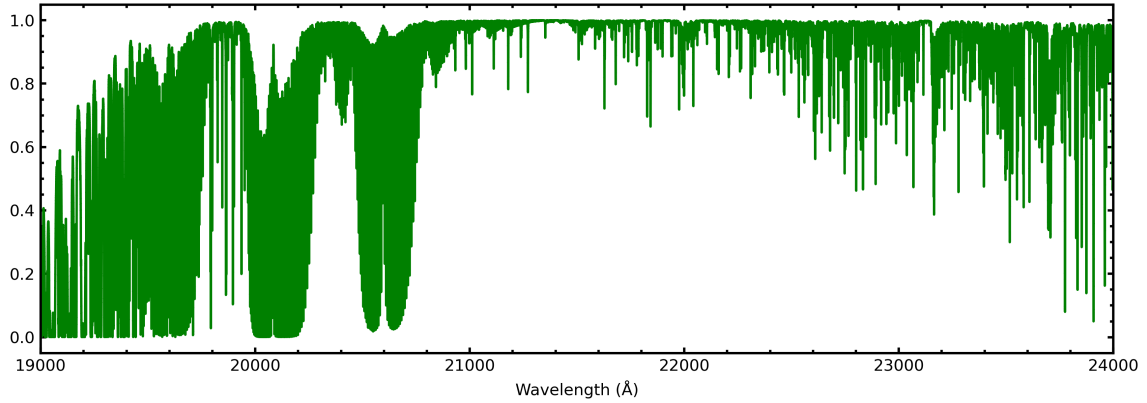


Figure 2.6: Synthetic telluric spectrum generated with the TAPAS portal, by specifying the proper observing date and site (i.e. Paranal) to realistically model the telluric absorption during the observations of each target star.

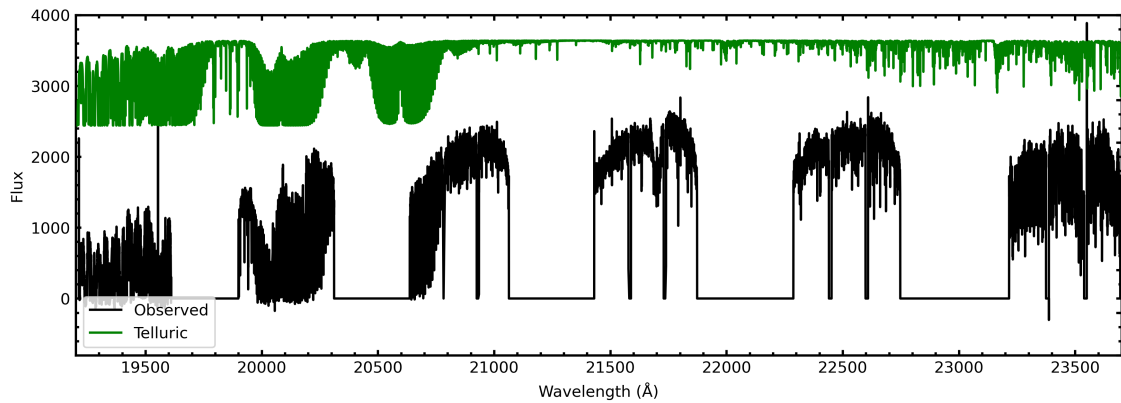


Figure 2.7: Pipeline-processed spectrum of a Liller 1 star (black line) that includes all the orders in the K2166 configuration. For comparison, the corresponding telluric spectrum (green line) computed with the TAPAS portal to be used for removing telluric absorptions from the target spectrum, is also reported.

Fig. 2.6 shows the K-band telluric spectrum computed with TAPAS at the selected resolution of $R=50,000$. Fig. 2.7 shows the full CRIFRES+ spectrum of a Liller 1 star, with the six spectral orders of the selected K2166 configuration clearly distinguishable, and for comparison, the telluric spectrum to be used for removing telluric absorptions from the observed star spectrum.

In the K-Band spectral range between 21000 and 24000 Å telluric absorption is mostly in the form of individual lines, while Earth's atmosphere is almost opaque below 21000 and above 24000 Å.

Whenever possible, regions of the spectrum that are particularly dense in telluric absorptions should be avoided for radial velocity and chemical abundance analysis. Indeed, in these regions, correction is not optimal and residuals can contaminate the spectral lines and affect the accuracy of the radial velocity and chemical abundance measurements.

Chapter 3

Spectral analysis

Stellar spectra are characterized by a continuum and by absorption features (either atomic lines or molecular lines/bands). The shape of the continuum of an observed spectrum is the convolution of the instrumental response (e.g. detector, echelle grating and cross-disperser efficiencies etc.) and the intrinsic energy distribution of the target source.

In order to measure accurate stellar parameters and chemical abundances of stars from their spectral lines, the observed spectra processed by the instrument pipeline need some additional treatment, namely spectrum normalization and correction for telluric absorption and heliocentric radial velocity.

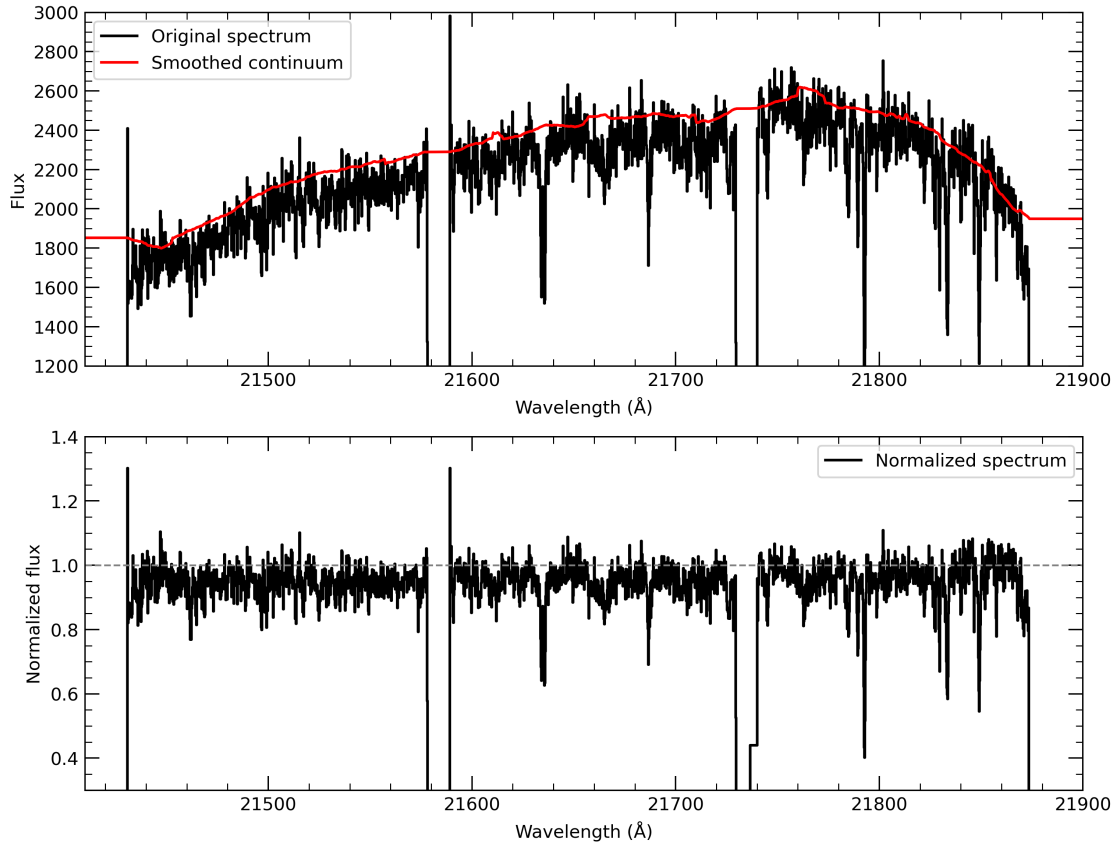


Figure 3.1: One order of the K-Band spectrum of a Liller 1 star centered at about 21700 Å before (top panel) and after (bottom panel) rectification and normalization of the continuum to 1.

3.1 Continuum normalization, telluric removal and radial velocity correction

The normalization of a stellar spectrum is a critical step since chemical abundances are derived from the measurement of the absorption line profile and equivalent width relative to the continuum, and the uncertainty in its positioning can significantly impact the derived values.

The continuum normalization is a particularly challenging task in case of cool stars, since their spectra are densely populated of metallic lines and molecular bands.

Typically, continuum normalization foresees a first global pre-normalization via polynomial fitting and/or low-pass filtering (e.g. smoothing) of the full spectrum. Then a local (i.e. around each line of interest) adjustment, by using suitable synthetic stellar spectra as reference, is performed, to optimally determine the continuum of each measured line.

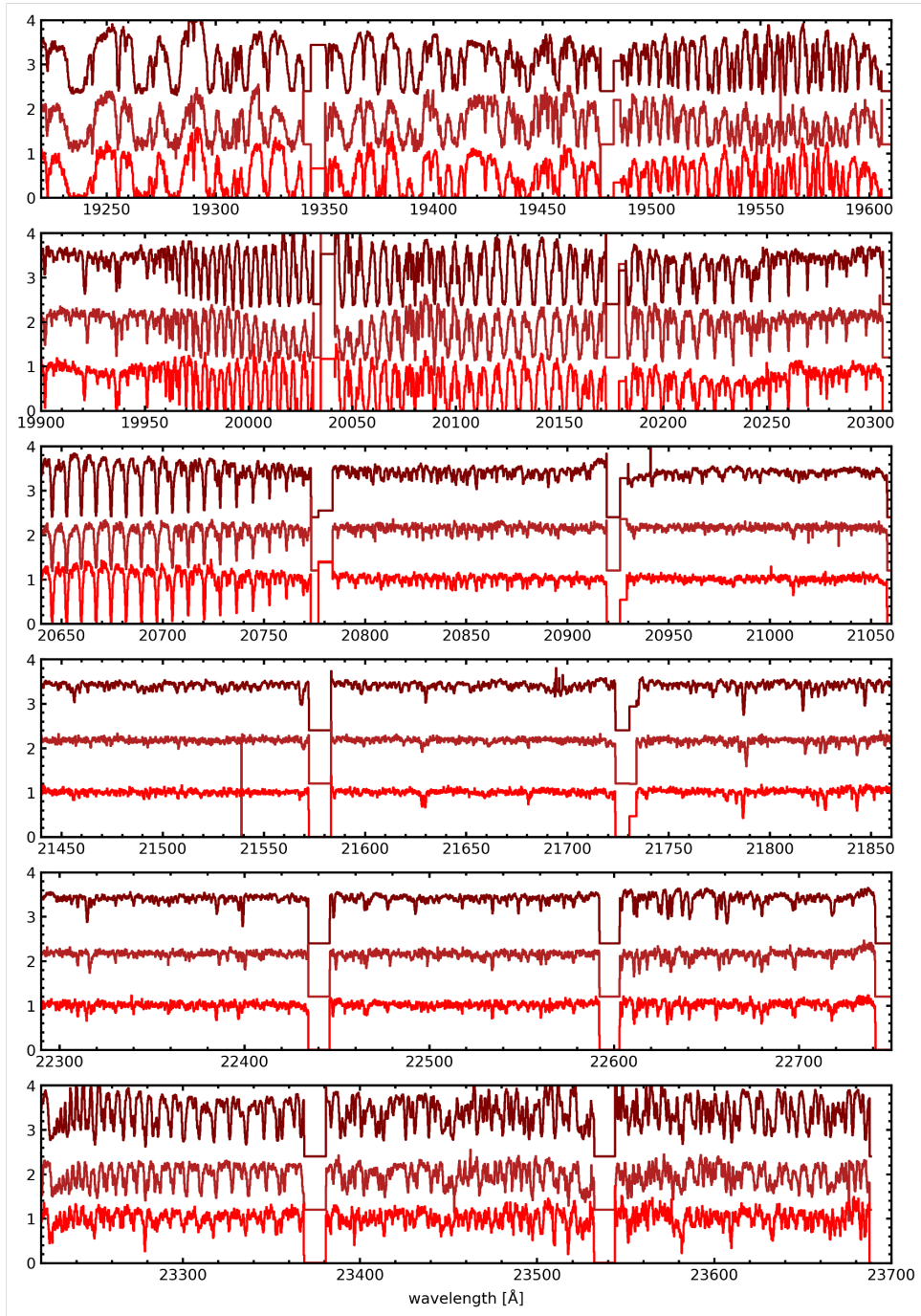


Figure 3.2: Rectified and normalized CRIFES+ spectra in the K2166 configuration, with all the observed orders along the Y-axis, of three representative Liller 1 giant stars with different temperatures: $T_{eff} \approx 3200$ K (top spectra in each panel), $T_{eff} \approx 3600$ K (middle spectra in each panel) and $T_{eff} \approx 4100$ K (bottom spectra in each panel). In each spectrum the gaps in between the three detectors are clearly visible.

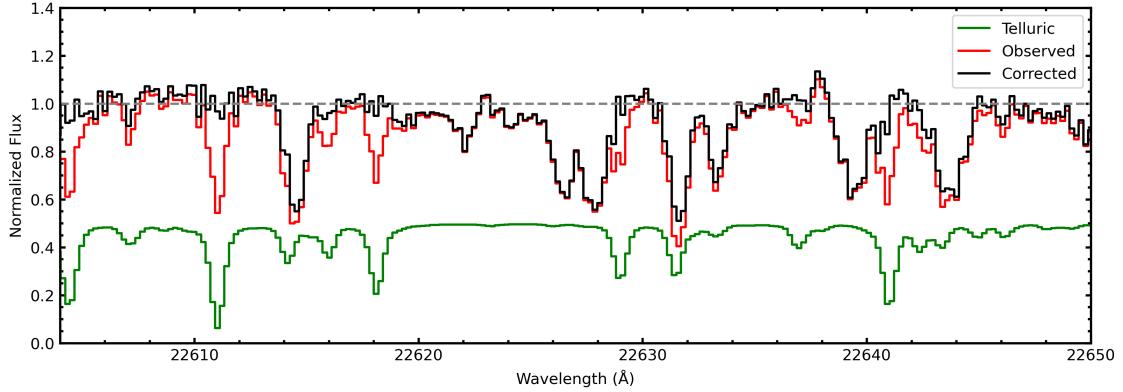


Figure 3.3: Removal of telluric absorption lines from the spectrum of an observed RGB star in Liller 1.

In order to rectify and normalize the CRIFES+ K-band spectra a smoothing low-pass filtering is applied to each order of the spectrum, using a smooth filter size of a few hundreds pixels, i.e. about 5% of the total number of spectral pixels (about 6000 for each order).

As an example, Fig. 3.1 shows one order of the K-Band spectrum of a Liller 1 star before and after rectification and normalization of the continuum to 1, while Fig. 3.2 shows the full, normalized spectra of three representative Liller 1 stars with different temperatures. It is worth noticing that the spectral region at $\lambda < 20800 \text{ \AA}$ is largely dominated by strong telluric absorptions.

After a proper normalization, the spectrum has to be corrected for telluric absorption, by dividing it for normalized telluric spectrum (see Sect. 2.2).

An example of a CRIFES+ spectrum before and after the telluric correction is shown in Fig. 3.3. The final, normalized and telluric corrected spectra are ready to be ingested by the science pipelines in order to get radial velocity and chemical abundance measurements for the observed stars.

3.2 Radial velocity

Stars have line-of-sight radial motions with respect to the observer, causing Doppler blue or red shifts of their spectral lines, depending on whether the star is moving towards or away from the observer, respectively.

Radial velocities, accurate to within 1 km s^{-1} , were determined using a conventional cross-correlation (Lockwood et al., 2014) technique between the observed and suitable synthetic spectra, which have zero velocity by construction, and stellar parameters resembling those of the observed stars.

The observed spectrum is kept fixed while the synthetic ones are slid across the fixed spectrum pixels, in search of the best match. A correlation probability is computed, yielding the cross-correlation function, whose peak corresponds to the best-fit velocity solution. In order to derive the radial velocities of the 12 stars of Liller 1, the 22290-22410 Å portion of their K-band spectra has been used, since it contains a number of bright and sufficiently isolated absorption lines for precise and accurate measurements of their centroids. To the inferred radial velocities the heliocentric correction has been applied, in order to take into account the motion (specifically, the component of its velocity along the line of sight) of the Earth with respect to the Sun and to the barycenter of the Solar system. The normalized and telluric-corrected spectra are thus finally corrected for heliocentric radial velocity, in order to have rest-frame spectra to be directly compared with synthetic stellar spectra spanning a wide range of stellar parameter and chemical abundances.

3.3 Effective temperature and surface gravity

Temperature and gravity are among the most important parameters to be determined, since they play a fundamental role in shaping the continuum and absorption lines of stellar spectra, with a consequent major impact in the derived chemical abundances.

A first guess of the stellar temperature and gravity has been obtained photometrically, by projecting each studied star on a suitable isochrone from the set of Bressan et al. (2012) that reasonably match the observed CMD. An isochrone is an instantaneous picture, i.e. at a fixed age, of the distribution in the theoretical temperature-luminosity plane (Hertzsprung-Russell diagram) or, equivalently, in the observational color-magnitude plane of stars with different initial masses at a given metallicity.

An iterative procedure has been adopted, starting with the assumption that all the studied stars of Liller 1 belong to the main, old, sub-solar stellar sub-population, and we projected them on an isochrone of 12 Gyr and with a metallicity of -0.3 dex, thus deriving the corresponding temperature and gravity.

We then used these temperature and gravity values for a first computational run of the chemical abundances of iron and α -elements from the CRIRES+ spectra. For those stars for which the resulting abundances were significantly different from those of the reference sub-solar sub-population, and in particular significantly more metal-rich, the procedure has been repeated, by 1) re-projecting their position in the CMD on an isochrone better describing the young, super-solar sub-population of Liller 1, namely 2 Gyr old and with a metallicity of +0.3 dex; 2) re-determining their temperature and gravity, and 3) finally re-computing their chemical abundances.

However, it is worth mentioning that impact of the chosen isochrone on the derived temperatures and gravities of the Liller 1 stars is not dramatic, with temperatures varying by less than 100 K and gravities by about 0.3 dex, with an overall impact on the derived abundances of less than 0.1 dex.

Although the number of available iron lines is not large, as a sanity check, we also verified whether any significant trend in the derived iron abundance from individual Fe I lines as a function of excitation potential was present.

3.4 Micro- & Macro- turbulence velocities

Spectral lines are intrinsically broadened by thermal and turbulent motions of the atoms and molecules in the photospheric gas. At a given temperature and under the condition of local thermal equilibrium, the velocities of the atoms and molecules are characterized by a Maxwellian distribution with a dispersion $\Delta v_{thermal}$ given by the formula

$$\Delta v_{thermal} = \sqrt{\frac{2KT}{m}}$$

where K is the Boltzmann constant, T the gas temperature, m the atomic mass of the studied chemical element. In cool stars thermal broadening alone (typically $\leq 1-2 \text{ km s}^{-1}$) is not sufficient to model the line core width, hence an additional velocity component, named micro-turbulence, is added in quadrature to the Doppler broadening. Hence the total line core broadening Δv in velocity units is described by the following formula

$$\Delta v = \sqrt{\frac{2KT}{m} + \xi^2}$$

where ξ is the microturbulence velocity.

The standard method for setting microturbulence is to find the value that minimizes any trend between $[\text{Fe}/\text{H}]$ and the so-called reduced equivalent width (EW), i.e. $\log_{10}(\text{EW}/\lambda)$. In giant stars microturbulence can typically vary from 1 to 3 km s^{-1} , higher values in cooler and more luminous stars.

The modeled spectra need to be convoluted to the spectral resolution of the observed spectra. Normally, the observed spectra of giant stars turn out to be broader than the nominal resolution of the echelle spectrograph, given by $R = \frac{c}{v_{instr}}$, where c is the light speed and v_{instr} is the instrumental broadening in velocity units. This is attributed to turbulent motions of the gas cells, whose size is greater than the mean free path of a photon. This additional broadening is named macro-turbulence, and it is normally modeled with a Gaussian profile, as the instrumental one.

3.5 Chemical analysis

Chemical analysis of the observed spectra has been performed by means of spectral synthesis techniques, by using a suitable grid of synthetic spectra with stellar parameters representative of the target stars and abundances varying over the wide range spanned by the Liller 1 stellar populations.

Synthetic spectra have been generated by using the radiative transfer code Turbospectrum (Alvarez and Plez, 1998; Plez, 2012), under the Local Thermal Equilibrium (LTE) approximation, the MARCS models atmospheres (Gustafsson et al., 2008), the atomic data from VALD3* and the most updated molecular data from B. Plez website†.

In particular, for each observed star, a set of synthetic spectra, with fixed stellar parameters (i.e. with T_{eff} , $\log(g)$, and micro and macro turbulence representative of the selected star), with $[\text{Fe}/\text{H}]$ varying from -1 to +0.5 dex, with an increment of 0.1 dex, and with both solar-scaled as well as with some enhancement of $[\alpha/\text{Fe}]$ and $[\text{N}/\text{Fe}]$ and depletion of $[\text{C}/\text{Fe}]$, have been computed.

The reason to have also synthetic spectra with $[\alpha/\text{Fe}]$, $[\text{N}/\text{Fe}]$ and $[\text{C}/\text{Fe}]$ abundance ratios that deviate from solar-scaled ones is that these elements can impact the resulting continuum opacity and molecular equilibria.

The spectral synthesis technique foresees the comparison of observed and synthetic spectra through specific figures of merit, namely statistical tools like e.g. the minimization of the χ^2 of the distribution, if a sufficient number of spectral elements/pixels are available, and/or the line strength (either its equivalent width or its depth, depending on the line purity, symmetry etc.).

This technique is quite versatile and it can be applied to wide portions of spectra including several lines as well as to individual lines of interest.

Some more information on the computation of the synthetic spectra and the adopted spectral synthesis technique can be found in Appendix A.1.

*<http://vald.astro.uu.se>

†<https://www.lupm.in2p3.fr/users/plez/>

Table 3.1: List of neutral atomic lines of Fe, Mg, Si, S, Ca and Ti used to obtain chemical abundances.

Element	Wavelength (Å)	E.P. (eV)	log(gf)	log ₁₀ ϵ(X) _⊙
Fe I	21553.299	6.70	-0.500	7.50
Fe I	21813.977	5.85	-1.390	7.50
Fe I	21832.980	6.78	-2.166	7.50
Fe I	21851.381	3.64	-3.610	7.50
Fe I	21856.131	6.18	-1.320	7.50
Fe I	22375.178	5.84	-1.070	7.50
Fe I	22380.797	5.03	-0.460	7.50
Fe I	22385.102	5.32	-1.350	7.50
Fe I	22392.879	5.10	-1.250	7.50
Fe I	22419.977	6.22	-0.150	7.50
Fe I	22473.264	6.12	0.440	7.50
Fe I	22493.672	5.83	-0.890	7.50
Fe I	22619.838	4.99	-0.360	7.50
Mg I	21458.863	6.52	-1.320	7.55
Mg I	21536.520	6.78	-1.860	7.55
Mg I	23328.094	6.72	-1.490	7.55
Al I	22700.914	4.83	-1.490	6.43
Si I	21441.924	7.33	-0.300	7.59
Si I	21754.434	7.30	-0.670	7.59
Si I	21779.660	6.72	0.420	7.59
Si I	22423.100	7.32	-0.780	7.59
Si I	22537.533	6.62	-0.230	7.59
Si I	22665.758	6.62	-0.680	7.59
S I	22507.557	7.87	-0.480	7.16
S I	22519.066	7.87	-0.250	7.16
S I	22526.053	7.87	-0.510	7.16
S I	22563.828	7.87	-0.260	7.16
S I	22575.395	7.87	-0.730	7.16
S I	22644.057	7.87	-0.340	7.16
S I	22707.738	7.87	0.440	7.16
Ca I	22607.943	4.68	0.520	6.37
Ca I	22626.723	4.68	-0.220	6.37
Ca I	22651.178	4.68	0.850	6.37
Ca I	22653.578	4.68	-0.220	6.37
Ti I	21532.820	3.90	-0.700	4.94
Ti I	22310.617	1.73	-2.070	4.94
Ti I	22443.926	1.74	-2.360	4.94
Ti I	22621.221	1.75	-2.740	4.94
Ti I	22632.742	1.88	-2.760	4.94

Note: Solar reference abundance log₁₀ϵ(X)_⊙ from Magg et al. (2022).

A suitable line list for the chemical analysis has to be defined and optimized, according to the spectral range, stellar properties and spectral resolution of the observed spectra. Line selection was initially guided by existing works in the literature (Afşar et al., 2018; Fanelli et al., 2021, 2022; Lim et al., 2022).

Subsequently, a few other clean lines, as selected from VALD3[‡], NIST[§], and Kurucz[¶] databases and visually inspected on both synthetic and observed spectra, have been added to the list since safely measurable at the CRIRES+ resolution.

Table 3.1 lists wavelengths and atomic parameters of all the lines used in this Thesis work for the chemical abundance analysis of the 12 selected stars of Liller 1.

About 40 neutral atomic lines of Fe, Mg, Si, S, Ca and Ti have been selected since suitable for being measurable in the K2166 CRIRES+ spectra and whose strength is reasonably sensitive to abundance variations of the corresponding chemical specie.

These lines are sufficiently isolated from strong telluric absorptions, poorly contaminated by nearby lines and un-saturated, thus maximizing their sensitivity to abundance variations.

Spectral synthesis has been performed around each selected individual line, by using as a figure of merit their strength, which depends both on its excitation potential and transition probability, that are fixed parameters characterizing that specific atomic or molecular transition, but also on the gas properties (temperature, density etc.) and chemical content of the stellar atmosphere.

Line strengths have been computed by integrating the line flux within its core profile, only, in order to maximize the probability to be dominated by the specie responsible for that transition, and avoiding the line wings that can be more easily contaminated and/or dominated by the contribution of nearby small lines.

The same spectral sampling and line strength definition have been used to measure the selected lines in both the observed and synthetic spectra in order to avoid possible systematic biases.

[‡]<http://vald.astro.uu.se>

[§]<https://www.nist.gov/pml/atomic-spectra-database>

[¶]<http://kurucz.harvard.edu>

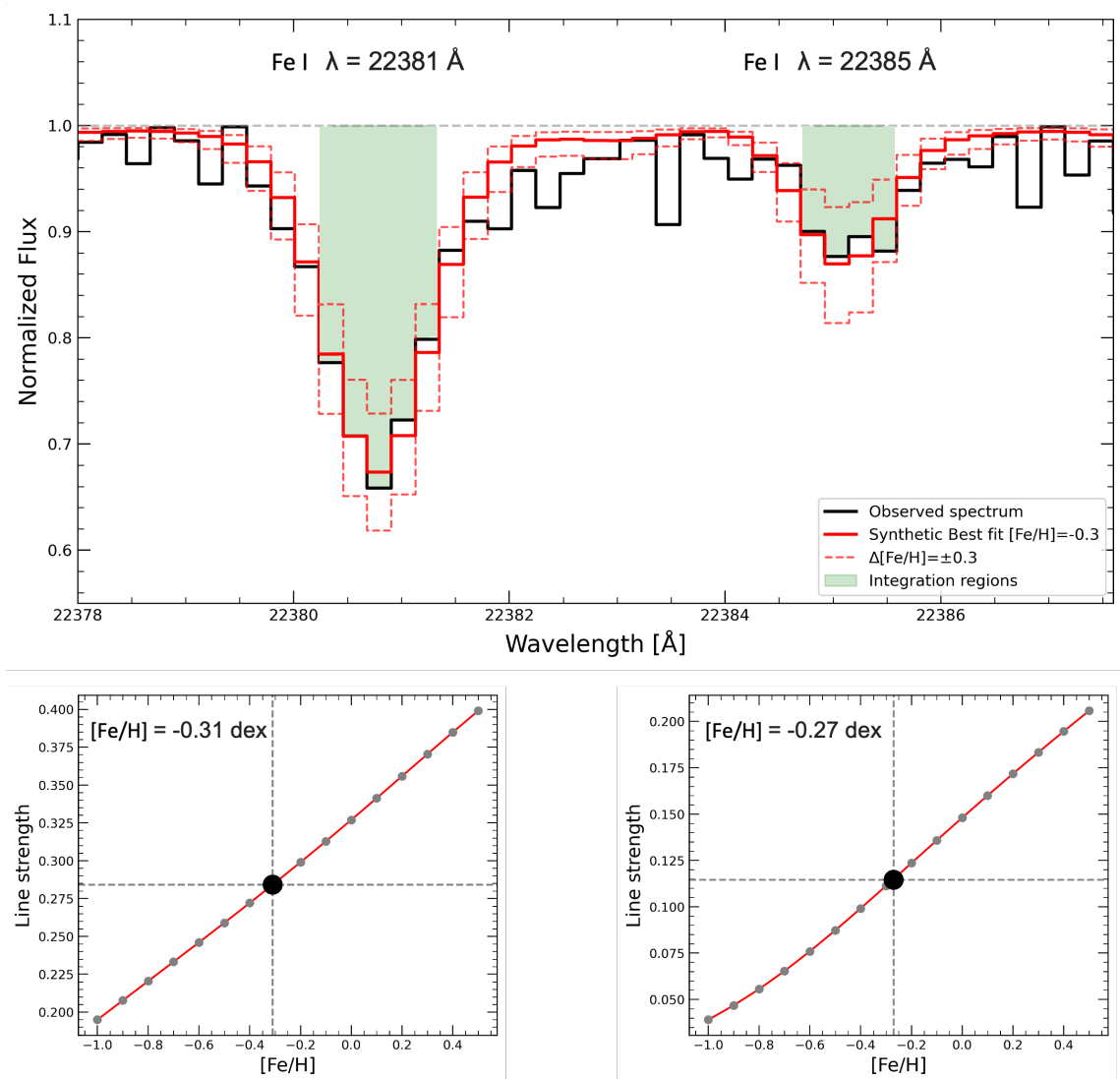


Figure 3.4: Line strength measurement of the Fe I lines at 22380.797 \AA and 22385.102 \AA . Top panel: observed spectrum (black line), best-fit synthetic spectrum (red line), and other two spectra with ± 0.3 dex with respect to the best fit (dotted, red lines). The shaded areas indicate the core regions where the line strengths have been computed. Bottom panels: pseudo-curve-of-growth for the two iron lines, as constructed by interpolating the line strength measurements in the set of synthetic spectra that have the same stellar parameters of the observed star spectrum and with the element abundance varying in the selected range between -1.0 and $+0.5$ dex, in step of 0.1 dex. The positions in which the measured line strengths in the observed spectra intersect pseudo-curve-of-growths are marked as black big dots.

In order to get the chemical abundances, for each selected line, a pseudo curve-of-growth is built up by interpolating the line strength measurements in the set of synthetic spectra that have the same stellar parameters of the observed star spectrum and with the element abundance varying in the selected range between -1.0 and +0.5 dex, in step of 0.1 dex. The X-axis coordinate at which the line strength of the observed spectrum intersects such a curve-of-growth is the abundance solution for that line.

Fig. 3.4 schematically illustrates the measurement of the line strength of two selected iron lines.

Chapter 4

Results

The physical and chemical information for the 12 stars of Liller 1 analyzed in this Thesis work, as obtained from the analysis of the CRIRES+ spectra, are listed in Table 4.1. In particular, for each star, the inferred temperature, gravity, heliocentric radial velocity, iron abundance and abundance ratios of [Mg/Fe], [Al/Fe], [Si/Fe], [S/Fe], [Ca/Fe] and [Ti/Fe] are reported.

Table 4.1: Stellar parameters, radial velocities and abundances for the analysed sample of stars in Liller 1.

ID	T_{eff} K	$\log(g)$	v_{hel} km s^{-1}	[Fe/H] dex	[Mg/Fe] dex	[Al/Fe] dex	[Si/Fe] dex	[S/Fe] dex	[Ca/Fe] dex	[Ti/Fe] dex
400087	3210	0.3	84.4	0.26	0.03	0.03	-0.01	0.10	0.00	0.09
300097	3370	0.1	68.6	-0.47	0.28	0.28	0.31	0.47	0.38	0.33
200119	3480	0.3	66.5	-0.43	0.34	0.43	0.36	0.43	0.44	0.50
100157	3600	0.5	79.2	-0.25	0.33	0.24	0.23	0.48	0.28	0.20
300162	3600	0.5	57.0	-0.34	0.38	0.32	0.32	0.39	0.38	0.37
200179	3600	0.9	69.7	0.28	0.06	0.11	-0.04	0.07	0.00	0.14
400476	3980	1.5	50.8	0.25	0.10	-	0.00	0.03	0.04	0.07
400519	4040	1.3	64.1	-0.28	0.32	0.36	0.28	0.33	0.31	0.38
100689	4140	1.5	71.1	-0.33	0.38	0.44	0.36	0.43	0.34	0.36
400733	4160	1.5	65.2	-0.28	0.45	0.32	0.20	0.37	0.22	0.27
400860	4210	1.9	75.6	0.25	0.04	0.11	-0.01	0.08	0.03	0.15
100571	4250	1.6	66.8	0.22	0.03	0.11	0.00	0.04	0.05	0.15

4.1 Line-of-site kinematics

Radial velocities provide crucial information of the line of sight kinematics of the stellar system under investigation, and when combined with proper motions, a comprehensive 3D velocity map can be obtained.

For the 12 stars analysed in this Thesis work, heliocentric radial velocities fully consistent with the systemic one of 68 km s^{-1} and the 1σ dispersion of 7.3 km s^{-1} inferred by Crociati et al. (2023) have been found, as shown in Fig. 4.1.

These measurements provided the confirmation at high spectral resolution that the studied stars are likely members of Liller 1, hence representative of its stellar sub-populations.

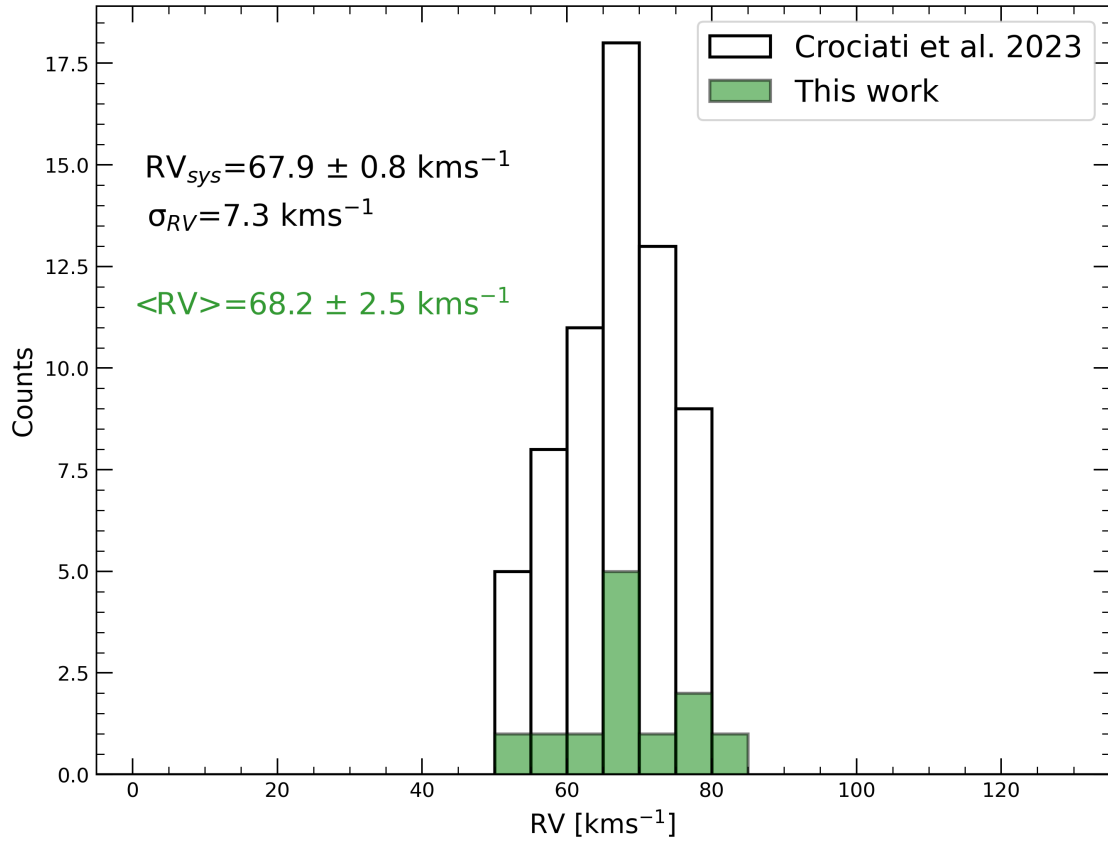


Figure 4.1: Distribution of radial velocities with reported the mean value and its error measured in this work (green histogram), overplotted to the distribution of Crociati et al. (2023) (empty histogram), with their estimated systemic radial velocity and velocity dispersion.

4.2 Stellar parameters

For the analyzed stars in Liller 1, we found that the spectral line core profiles can be reasonably fitted with a microturbulence velocity of 2 km s^{-1} and an overall line width with a macroturbulence velocity of about 10 km s^{-1} .

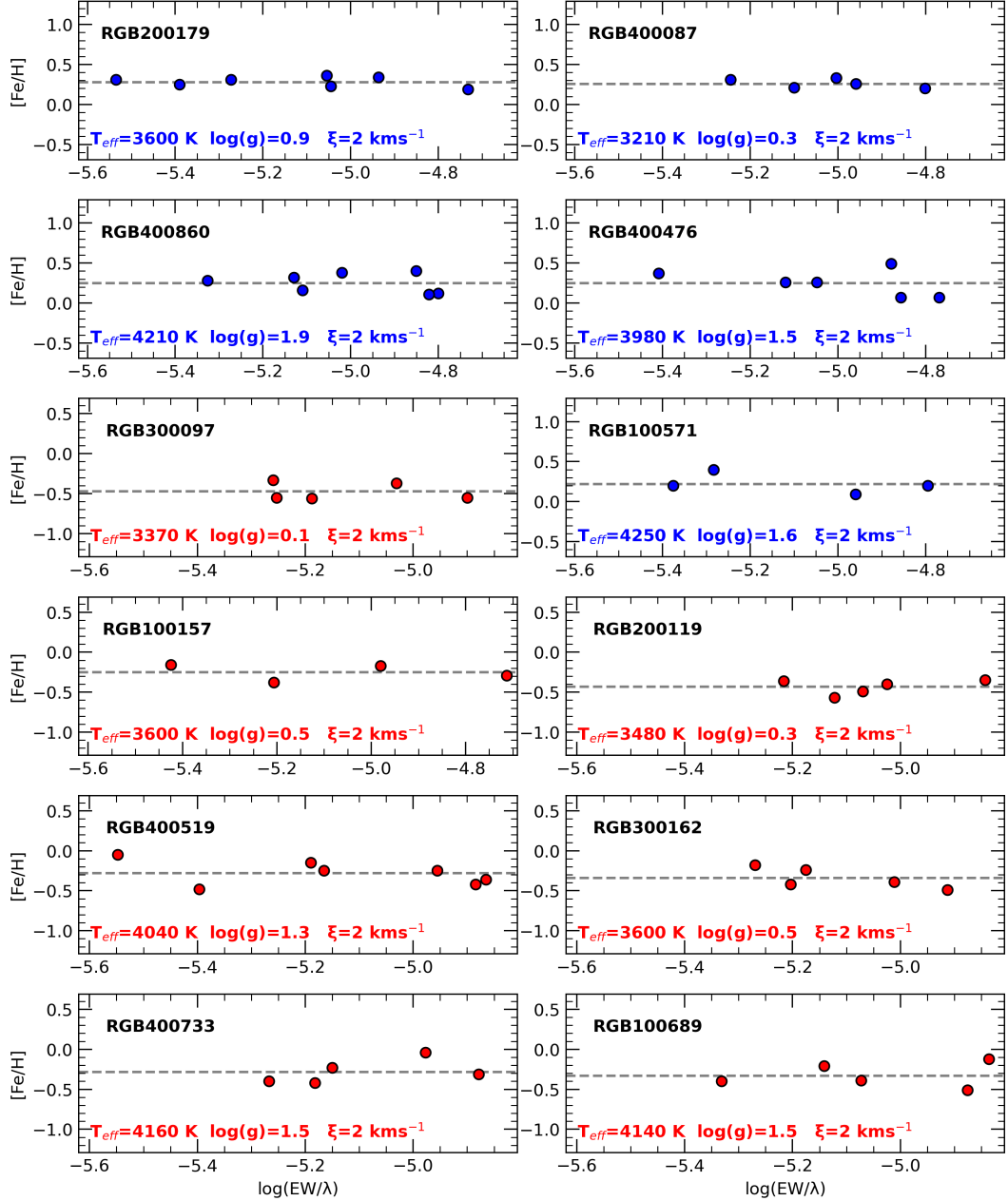


Figure 4.2: Iron abundances from Fe I lines as a function of their reduced EWs for the analyzed metal-poor (in red) and metal-rich (in blue) stars. Dashed lines mark the computed median iron abundance.

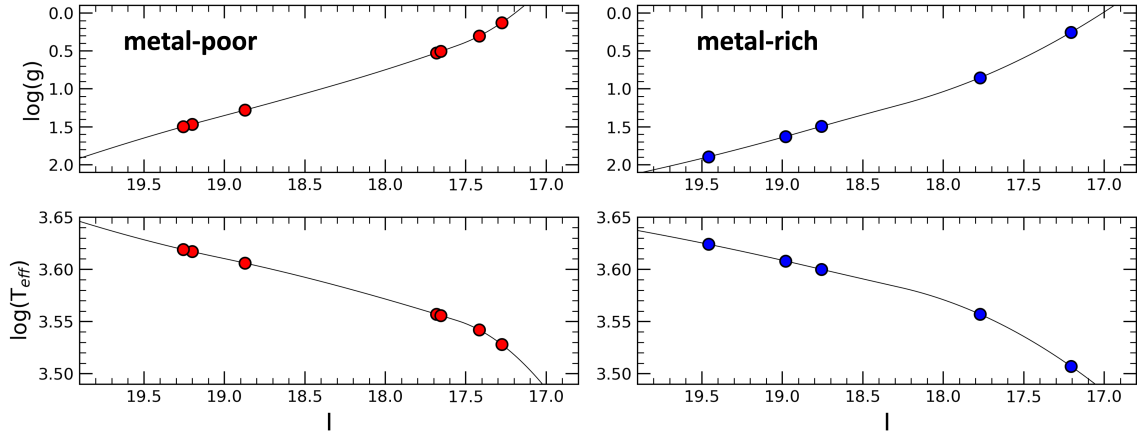


Figure 4.3: Estimated photometric temperatures and gravities as a function of the HST I-band magnitude (see Table 2.1 and Fig. 2.1) corrected for differential reddening for the analyzed metal-poor (left panels) and metal-rich (right panels) stars of Liller 1.

Although only from a few to a dozen iron lines could be measured, we nevertheless checked spectroscopically that the adopted microturbulence of 2 km s^{-1} be consistent with no significant trend between the measured line reduced EWs and the inferred iron abundances.

As shown in Fig. 4.2, the iron abundances from the various lines are randomly scattered around the median value, without any significant trend with the line reduced EW.

Effective temperatures T_{eff} in the 3200 - 4300 K range with $\pm 100 \text{ K}$ uncertainty and gravities $\log g$ in the 0.1 - 1.9 dex range with $\pm 0.2 \text{ dex}$ uncertainty have been photometrically derived (see Fig. 4.3) by projecting each studied star on a suitable isochrone that reasonably fits the observed CMD, as detailed in Sect. 3.3.

The overall impact of these uncertainties, mostly systematic, on the inferred chemical abundances listed in Table 3.1 is typically of $\approx 0.1\text{-}0.2 \text{ dex}$.

Photometric temperatures have been also checked spectroscopically, by verifying that there is not any significant trend between the inferred iron abundances and the excitation potential of the used lines.

As shown in Fig. 4.4 and similarly in Fig. 4.2, the iron abundances from the various lines are randomly scattered around the median value, without any significant trend with the line excitation potential.

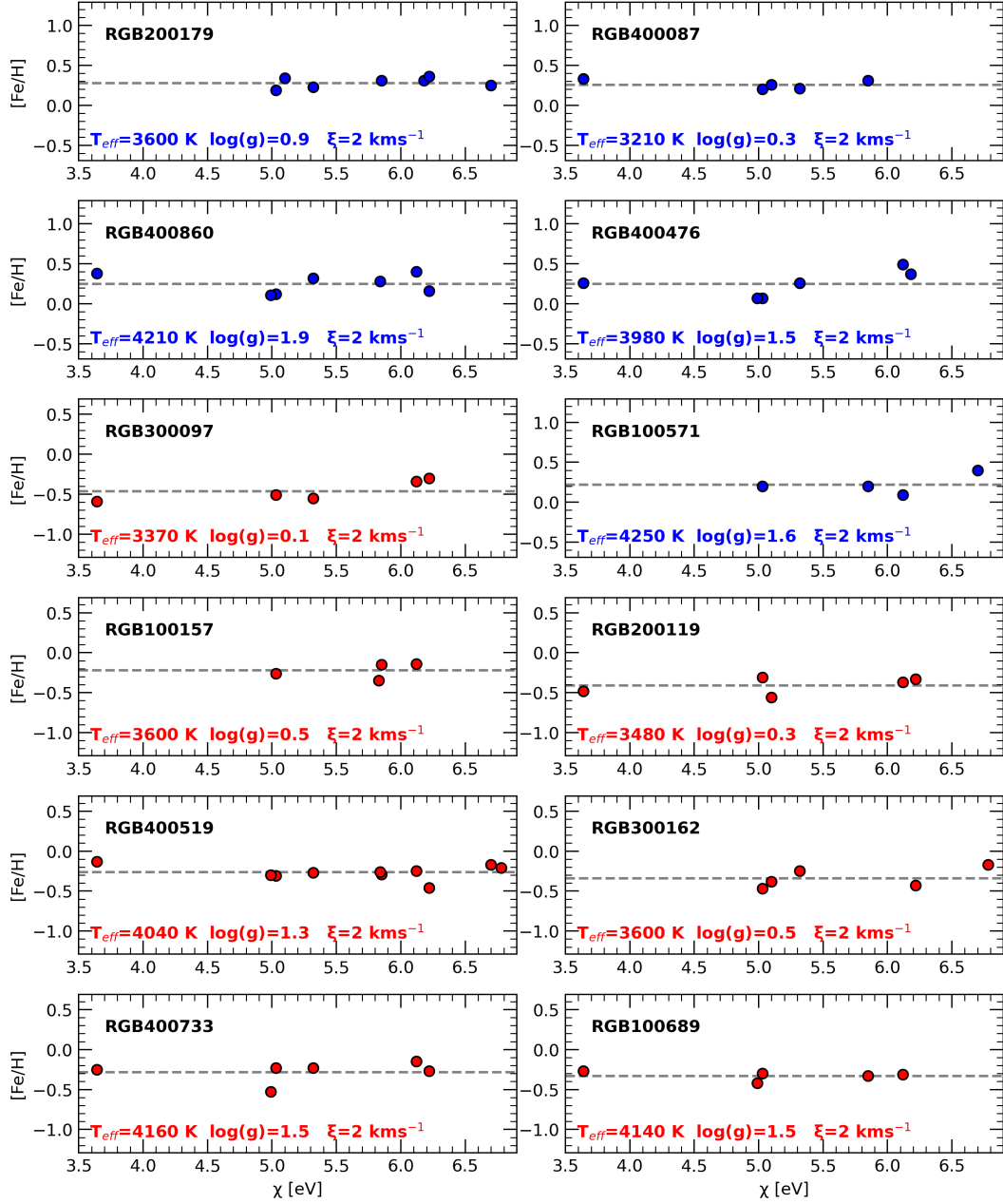


Figure 4.4: Iron abundances from Fe I lines as a function of their excitation potential for the analyzed metal-poor (in red) and metal-rich (in blue) stars. Dashed lines mark the computed median iron abundances.

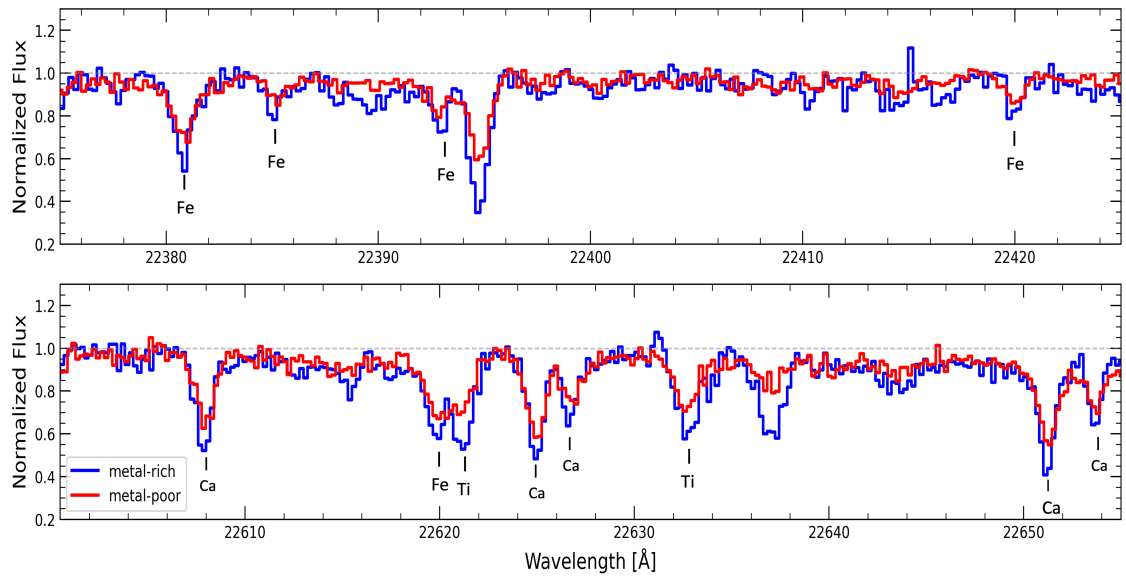


Figure 4.5: Portions of the K-band spectra of two analysed stars with similar T_{eff} but different chemical abundances (red line for the metal-poor star, blue line for the metal-rich one). A few atomic lines of interest are also marked.

4.3 Chemical abundances

The detailed chemical abundances of Fe, Mg, Al, Si, S, Ca and Ti for all the 12 observed stars of Liller 1, as listed in Table 4.1, have been derived from spectral synthesis of the atomic lines reported in Table 3.1.

Random errors in the derived abundances are mostly due to the uncertainty in the continuum positioning (typically such an uncertainty amounts to 1-2%) and to the spectrum photon noise. For elements with more than one measurable line, we computed the error of the mean of the abundances from the different lines, which typically amounts to a few hundredths of a dex, while the dispersion is typically 0.1-0.15 dex. For those elements with one measurable line, only, a conservative 0.1 dex error has been assumed.

Seven stars turned out to be sub-solar in iron, with an average value of $[Fe/H] \approx -0.3$ dex. The other five stars of the analyzed sample turned out to be super-solar in iron, with an average value of $[Fe/H] \approx +0.3$ dex. The overall iron spread amounts to about 1 dex, thus providing the high spectral resolution confirmation to the wide metallicity distribution inferred by Crociati et al. (2023) from low resolution VLT-MUSE spectra in the Ca triplet region.

As an example, Fig. 4.5 shows portions of the observed K-band spectra of a metal-poor and a metal-rich star of Liller 1 with similar stellar parameters but different iron content, as demonstrated by the different line depths.

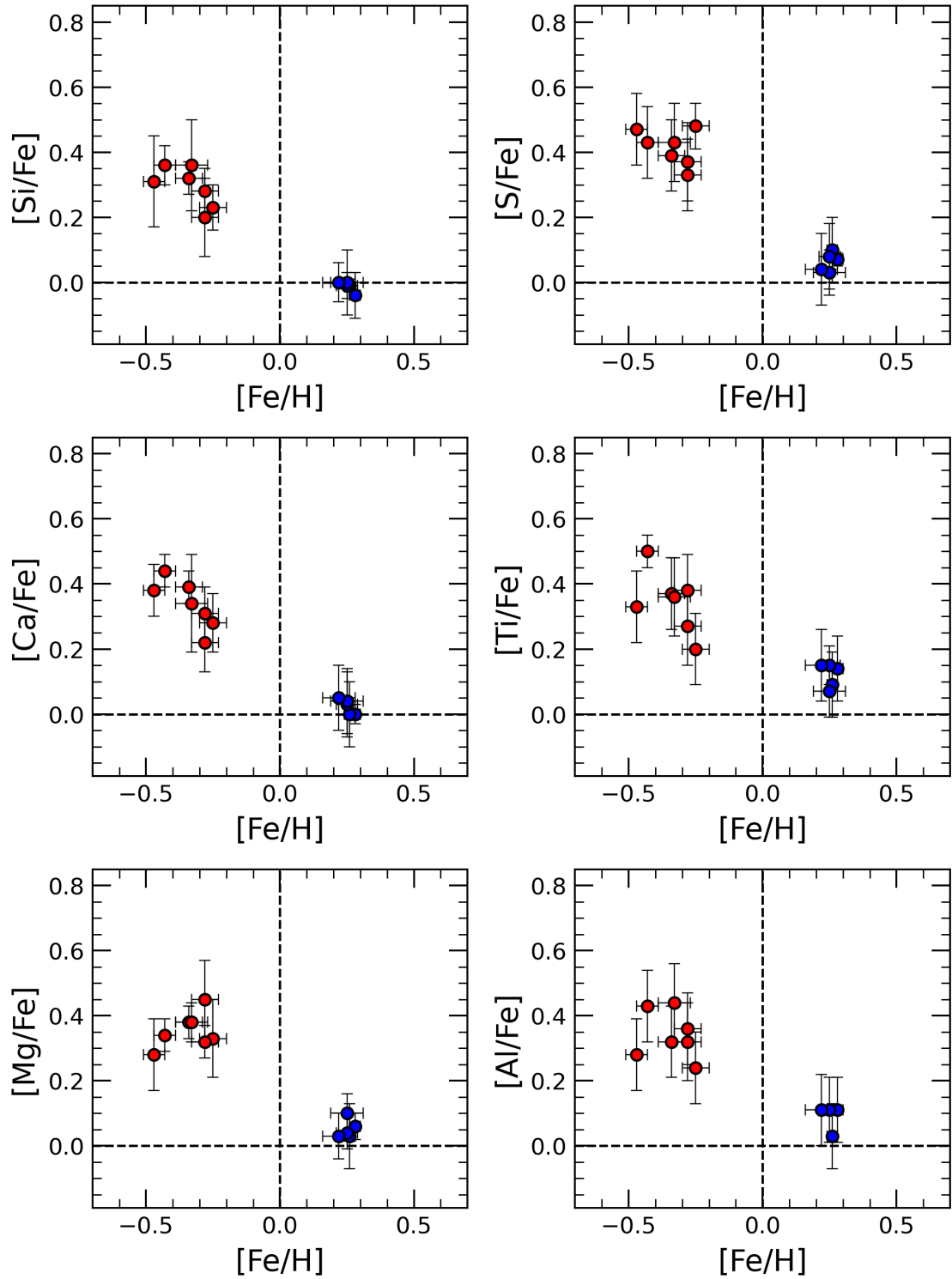


Figure 4.6: Individual $[X/Fe]$ abundance ratios of Mg, Al, Ca, Ti, Si and S as a function of $[Fe/H]$ for the metal-poor (red) and metal-rich (blue) analysed stars of Liller 1.

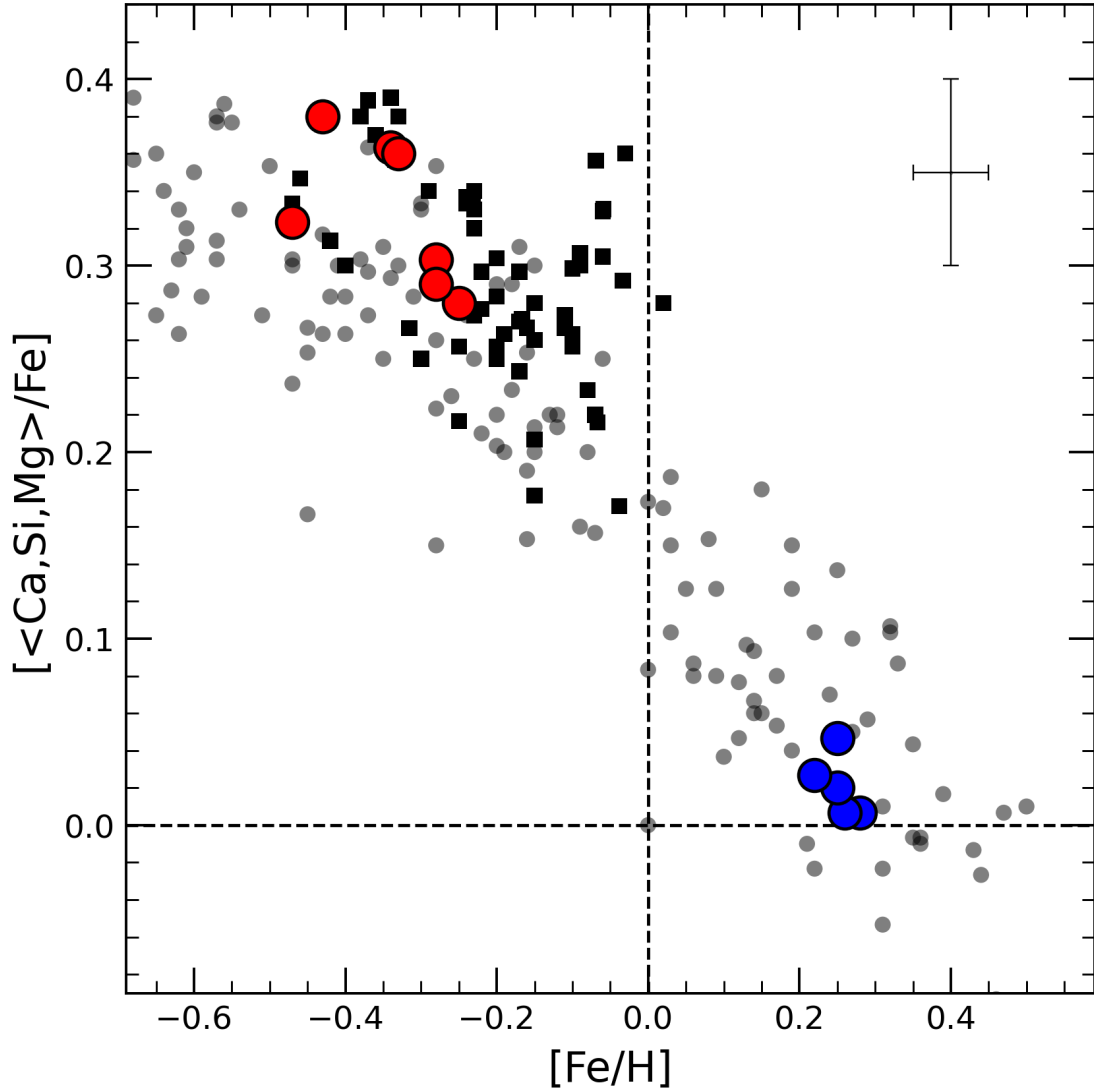


Figure 4.7: $[\langle \text{Ca, Si, Mg} \rangle / \text{Fe}]$ vs $[\text{Fe}/\text{H}]$ distribution for the metal-poor (red) and metal-rich (blue) analysed stars of Liller 1, with the typical errorbar plotted in the top-right corner. For comparison, the corresponding values for a sample of bulge giant stars from Rich et al. (2012) (black squares) and from Johnson et al. (2014) (grey dots) are also plotted. The typical error bar is marked on the top-right corner.

Fig. 4.6 shows the inferred $[\text{X}/\text{Fe}]$ abundance ratios of Mg, Al, Si, S, Ca and Ti as a function of the iron abundance for all the 12 analysed stars.

The sub-solar stellar sub-population shows an enhancement of all the measured $[\text{X}/\text{Fe}]$ abundance ratios with respect to the solar $[\text{X}/\text{Fe}]=0.0$ value. The average $[\text{X}/\text{Fe}]$ abundance ratios are within the 0.3-0.5 dex range.

Such a finding indicates that this sub-population should have formed quickly at the early epoch of the bulge formation from a gas mainly enriched by type II SN ejecta.

The super-solar sub-population show much smaller $[X/Fe]$ abundance ratios, with average $[X/Fe]$ between -0.1 and +0.1 dex for most of the measured elements.

Such a low (if any) α -enhancement suggests that this sub-population should have formed at later epochs with respect to the metal poor one, from a gas also enriched by type Ia SN ejecta.

From the abundance ratio distributions of Fig. 4.6 and Fig. 4.7 it appears quite clearly that Liller 1 hosts at least two main sub-populations with significantly different iron content and α -element enhancement, thus providing the first spectroscopic confirmation of the different metallicity and age of the double sequences in the observed CMD by Ferraro et al. (2021, see also Fig.1.4).

Such a distribution is strikingly similar to the one of Terzan 5 (see Fig. 1.3 and Origlia et al., 2011, 2013) and also resembles the bulge field one, as can be seen in Fig. 4.7, where the average $[\alpha/Fe]$ vs $[Fe/H]$ distribution of the Liller 1 stars is plotted against the corresponding values measured in bulge giant stars from Rich et al. (2012) and from Johnson et al. (2014), for comparison.

Chapter 5

Conclusions and future perspectives

The present Thesis work has provided the first detailed chemical screening of the Liller 1 stellar content based on high resolution spectroscopy in the near IR with CRIRES+ at the VLT.

Chemical abundances of Fe, Mg, Al, Ca, Ti, Si and S have been obtained for the brightest 12 stars in the observed sample. The analysis of the remaining 8 stars already observed with CRIRES+ (see Fig. 2.1) and the derivation of C and N abundances from the molecular CO and CN lines also present in the CRIRES+ spectra for the full sample of 20 stars will be performed in the next months.

The resulting chemical abundances for the 12 analysed stars indicate that Liller 1 hosts sub-populations with significantly different iron abundances (spread over about 1 dex) and $[\alpha/\text{Fe}]$ abundance ratios, enhanced at sub-solar metallicities and about solar-scaled at super-solar metallicities, similarly to Terzan 5, and formed through different star formation events over several Gyrs.

This first chemical study at high spectral resolution of Liller 1 is part of a larger project devoted to probe the early history of the Milky Way assembling through the chemical DNA of a representative sample of bulge globular clusters and more complex stellar systems like Terzan 5 and Liller 1.

255 hrs of observing time with CRIRES+ at the VLT has been granted to this project through the Large Program 110.24A4 (PI: F. Ferraro).

Observations with CRIRES+ in the H and J or K bands, depending on the reddening, of giant stars in Terzan 5, Liller 1 and other 14 bulge globular clusters are ongoing.

From these observations, a comprehensive set of iron, iron-peak (e.g. Mn, Co, Ni, Cr, V), alpha (Ca, Si, Mg, S, Ti) and a few other light elements (e.g. Al, Na, K) and some neutron-capture elements (e.g. Ce), will be measured from several dozens atomic lines, while CNO abundances will be obtained from CO, OH and CN individual molecular lines and bandheads.

This chemical screening will provide the necessary tool to constrain the stellar nucleosynthesis and chemical enrichment of these ancient and metal rich stellar systems and their true nature (i.e. genuine globulars or more complex stellar systems) and origin (i.e. in-situ versus accretion).

In particular, the acquisition of new, high resolution IR spectra of Terzan 5 and Liller 1 stars will enable to assess the chemical properties of their sub-populations and reconstruct their star formation and chemical enrichment history on a more robust statistical ground.

Liller 1 and Terzan 5 are indeed among the most massive stellar systems of the Galactic bulge, with a present day mass of a few $10^6 M_{\odot}$ (Ferraro et al., 2021; Lanzoni et al., 2010).

However, very likely, they were more massive (i.e. 10^7 - $10^8 M_{\odot}$) in the past, in order to have undergone a large number of type II SN explosions and thus to have been able to produce a large number of neutron stars that are needed to explain e.g. the huge population of millisecond pulsars in Terzan 5 and the huge collisional rate of Liller 1.

The Terzan 5 and Liller 1 detailed chemistry and 3D kinematics, that allowed to reconstruct their orbits, also indicate that they likely formed and evolved in-situ (i.e. in the bulge).

The recent modeling of the Terzan 5 chemical evolution (Romano et al., 2023) shows that a proto-Terzan 5 with a mass of a few $10^7 M_{\odot}$ should have been able to quickly form stars at the sub-solar metallicities of the old sub-populations and then, by retaining both the type II and type Ia SN ejecta, to self-enrich and forming stars at later epochs at the super-solar metallicity of the young sub-population. An analogous modeling of the Liller 1 chemical evolution will be soon performed when detailed chemical abundances for a more statistical significant sample of member stars will become available.

The evolutionary, chemical and kinematic information obtained so far are sufficiently comprehensive to support a scenario where the old sub-populations of Liller 1 and Terzan 5 could be candidate bulge fossil fragments of either seed clumps or remnants of more massive clumps, as observed in star-forming galaxies at high redshift, that did not fully dissolve to form the bulge, but likely evolved and self-enriched within it as independent sub-systems, that is with their own star formation and chemical enrichment history, depending also on their specific interactions with the local environment.

The younger sub-populations of Liller 1 and Terzan 5 could be the products of such an evolution.

The discovery and characterization of these intriguing stellar systems within the Galactic bulge, is further triggering the search of other candidates of bulge fossil fragments and also the debate about the formation of bulges/spheroids via some hierarchical assembly as other galaxy components.

Chapter **A**

Software Tools

This Appendix provides some additional information on the software tools developed and used in this Thesis work for chemical analysis, for the treatment of the observed spectra and for the testing of the adopted spectral synthesis technique.

A.1 Tools for chemical analysis

This section provide some details on the tools used to generate the grid of synthetic spectra and for the chemical analysis via the synthesis technique (see Sect. 3.5).

Synthetic spectra are generated using the Turbospectrum code, the MARCS model atmospheres, the VALD3 atomic line list and suitable molecular line list compilations (see Sect. 3.5).

The procedure for the computation of the synthetic spectra is schematized in the flux diagram of Fig. A.1.

A python wrapper named *santerre* has been used to read the input file *santerre.input* with all the necessary parameters to 1) compute the appropriate model atmosphere and 2) to run Turbospectrum in order to generate the desired set of synthetic spectra.

Model atmospheres consistent with the stellar parameters of the observed stars are obtained by interpolating the existing MARCS grid. To this purpose, the *santerre* wrapper calls the python wrapper *create_model* that launches the FORTRAN-based routine written by Thomas Masseron*, as suggested by the MARCS team, and adapted for a 3D (i.e. in temperature, gravity and metallicity) interpolation.

An example of the *santerre.input* file, including the selected stellar T_{eff} , $\log(g)$, $[Fe/H]$, $[\alpha/Fe]$, wavelength coverage, microturbulence, spectral resolution, spectral sampling, linelist file and $[X/Fe]$ abundance ratio file, is reported in Fig. A.2.

For each observed star, two sets of 16 synthetic spectra each, with fixed temperature, gravity and microturbulence (those appropriate to each star, see Table 4.1) and with $[Fe/H]$ abundance varying between values -1.0 and 0.5 dex with a step of 0.1 dex, have been generated: the first set has solar-scaled $[X/Fe]$ abundance ratios while the second set has enhanced $[\alpha/Fe]=+0.3$ dex. The former (solar scaled) have been used to compute the final abundances of the young, super-solar stars, while the latter (alpha-enhanced) has been used to compute the final abundances of the old, sub-solar stars.

Additional spectra with varying T_{eff} by ± 100 K, $\log g$ by ± 0.3 dex and ξ by ± 0.2 km s⁻¹ with respect to the adopted values have been also computed in order to explore the impact of the uncertainties of the stellar parameters on the derived abundances.

*<https://marcs.astro.uu.se/software.php>

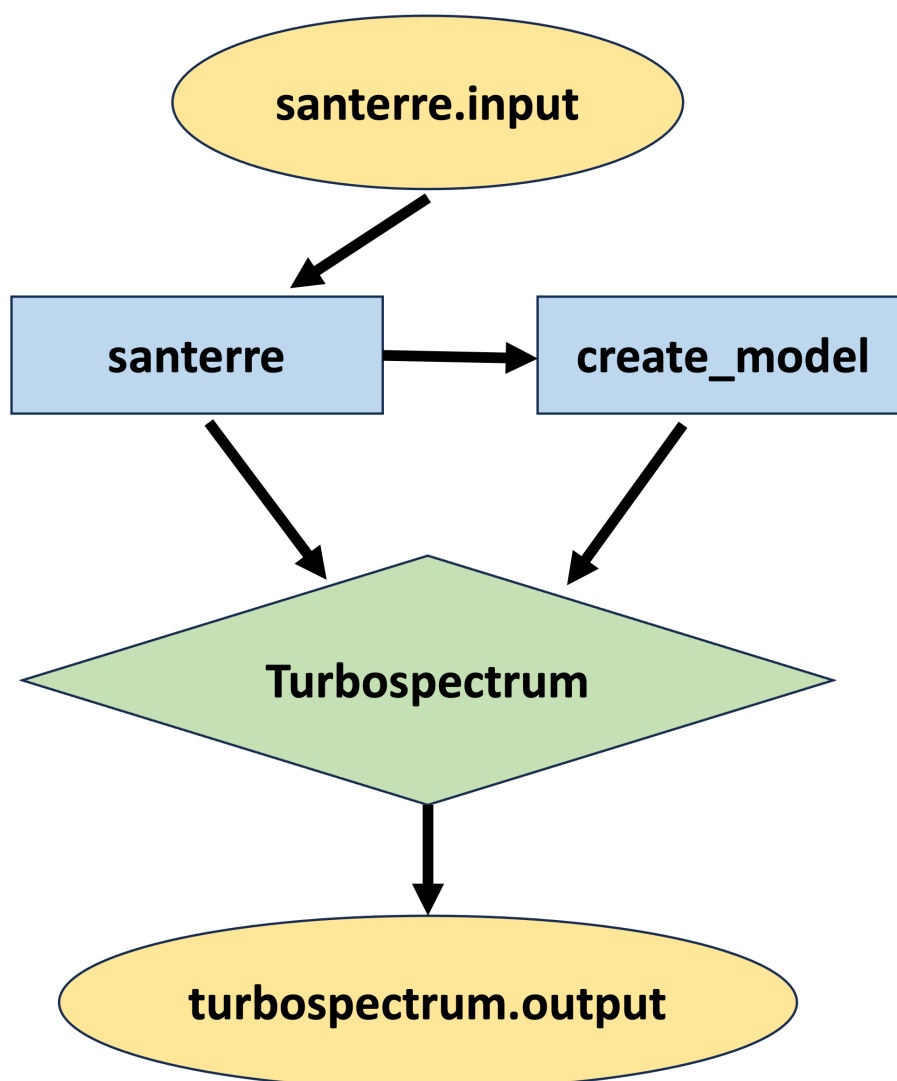


Figure A.1: Flux diagram of the procedure used for the computation of the synthetic spectra. Yellow ellipses indicate input/output files, blue rectangles refer to python wrappers, while the green diamond indicates the Turbospectrum code.

```

#Path where read/save input/output files

/read_save_path/
/LineList_path/
/Model_path/

# # #
#Stellar spectra
#Teff(K), log(g), [Fe/H],  $\lambda_i(\text{\AA})$ ,  $\lambda_f(\text{\AA})$ , xi(km/s), RES,  $\text{sample}(\text{\AA})$ ,  $\text{lineList\_file}(\text{str})$ ,  $\text{abu\_file}(\text{str})$ 
3600 0.9 -1.00 21000 23500 2.00 25000 0.10 linespecK.turbo abu.turbospec
3600 0.9 -0.90 21000 23500 2.00 25000 0.10 linespecK.turbo abu.turbospec
3600 0.9 -0.80 21000 23500 2.00 25000 0.10 linespecK.turbo abu.turbospec
3600 0.9 -0.70 21000 23500 2.00 25000 0.10 linespecK.turbo abu.turbospec
3600 0.9 -0.60 21000 23500 2.00 25000 0.10 linespecK.turbo abu.turbospec
3600 0.9 -0.50 21000 23500 2.00 25000 0.10 linespecK.turbo abu.turbospec
3600 0.9 -0.40 21000 23500 2.00 25000 0.10 linespecK.turbo abu.turbospec
3600 0.9 -0.30 21000 23500 2.00 25000 0.10 linespecK.turbo abu.turbospec
3600 0.9 -0.20 21000 23500 2.00 25000 0.10 linespecK.turbo abu.turbospec
3600 0.9 -0.10 21000 23500 2.00 25000 0.10 linespecK.turbo abu.turbospec
3600 0.9 +0.00 21000 23500 2.00 25000 0.10 linespecK.turbo abu.turbospec
3600 0.9 +0.10 21000 23500 2.00 25000 0.10 linespecK.turbo abu.turbospec
3600 0.9 +0.20 21000 23500 2.00 25000 0.10 linespecK.turbo abu.turbospec
3600 0.9 +0.30 21000 23500 2.00 25000 0.10 linespecK.turbo abu.turbospec
3600 0.9 +0.40 21000 23500 2.00 25000 0.10 linespecK.turbo abu.turbospec
3600 0.9 +0.50 21000 23500 2.00 25000 0.10 linespecK.turbo abu.turbospec

```

Figure A.2: An example of input file for the *santerre* wrapper with all the necessary parameters to compute the appropriate model atmosphere and to run Turbospectrum in order to generate the desired set of synthetic spectra.

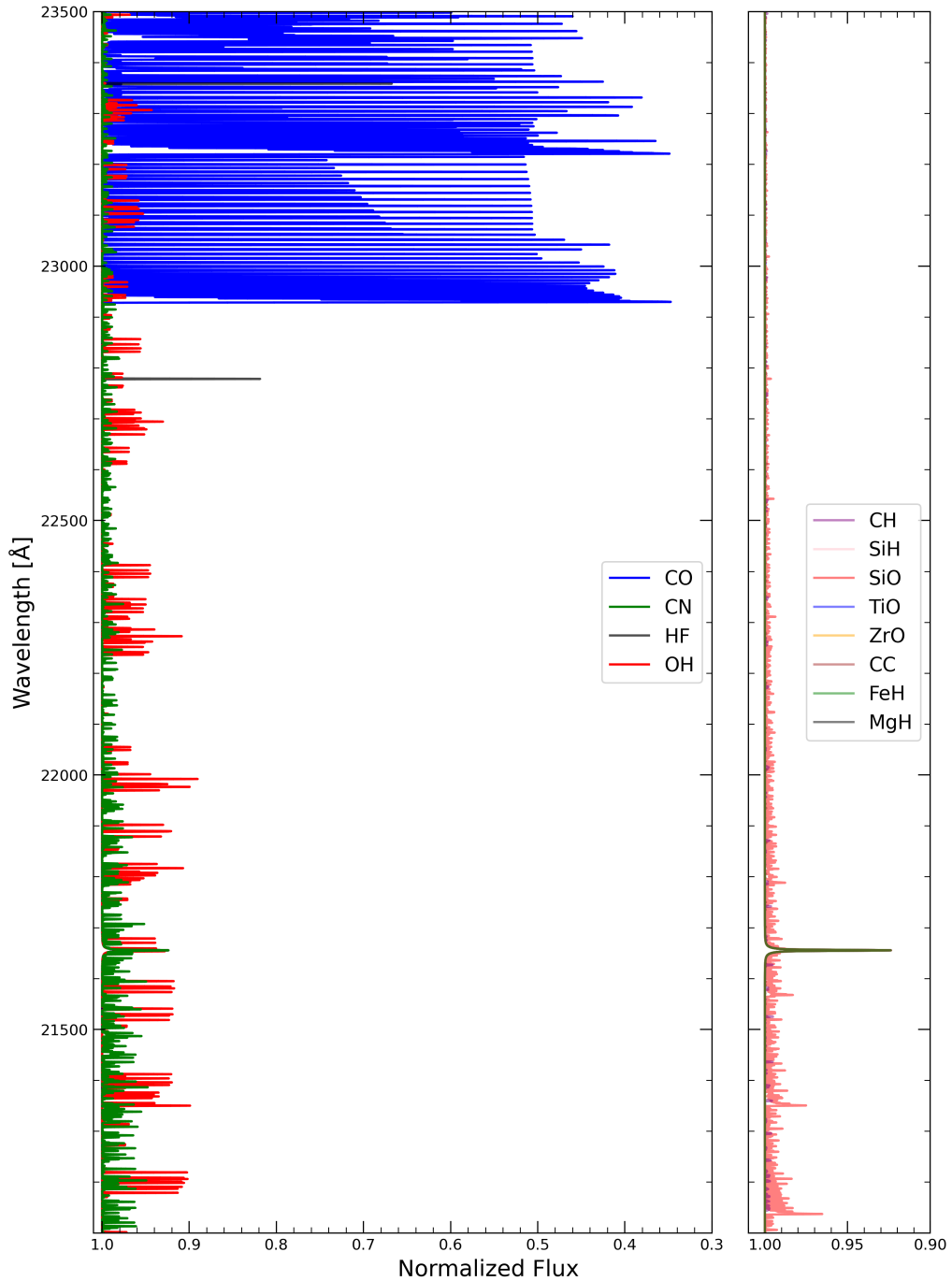


Figure A.3: Synthetic K-band molecular spectra for a $T_{eff}=3500$ K atmosphere for CO, OH, CN and HF with measurable lines (left panel) and for several other molecules listed in the legend with too shallow lines to be effectively measurable in the CRIRES+ spectra.

Once computed, these synthetic spectra have been convoluted with a Gaussian profile corresponding to an equivalent spectral resolution $R_{eq} \approx 25,000$ (i.e. 12 km s^{-1}), in order to take into account both the instrumental ($\text{FWHM}_{inst} = 6 \text{ km s}^{-1}$) and the macro-turbulence ($\text{FWHM}_{macro} \approx 10 \text{ km s}^{-1}$) broadenings (see Section 3.4) according to the relation:

$$R_{eq} = \sqrt{\left(\frac{c}{v_{inst}}\right)^2 + \left(\frac{c}{v_{macro}}\right)^2}$$

The following python script has been used to this purpose.

```
synth_file = pyasl.instrBroadGaussFast(wavelengths,flux,25000)
```

Before computing the thousand synthetic spectra needed for the chemical analysis of the 12 stars of Liller 1, we performed a few tests to identify areas where to save computational time. The huge number of molecular transitions turned out to have the most significant impact on the latter. Consequently, we carefully checked which molecular species have detectable transitions in the CRIRES+ K-band spectra, by computing the expected molecular spectra of a representative synthetic star.

As shown in Fig. A.3, CO has many deep lines at $\lambda \geq 22900 \text{ \AA}$ OH has several groups of fainter ($< 10\%$ of the continuum at $R_{eq} = 25,000$) lines, CN has faint ($< 5\%$ of the continuum) lines almost uniformly spread over the K band, while HF has only a few but deep lines. All the other molecules have normally very shallow ($< 2\%$ of the continuum, with the exception of one MgH and a few SiO transitions) lines even in coolest giants, hence they can be neglected. By including only the transitions of CO, OH, CN and HF, one can save $\geq 20\%$ of computational time when generating the synthetic spectra.

Line strengths in the observed and synthetic spectra have been measured by summing the flux of the few pixels around each line centroid as shown in Fig. 3.4. The line wings are avoided by purpose since possibly more contaminated by small nearby lines. For each star to be analysed, an input file listing the lines to be used for chemical analysis has been compiled. For each listed spectral line, together with the line wavelength and the chemical specie responsible of that transition, three additional parameters namely 1) the local normalization factor (default is 1) to refine the continuum level of the observed line, 2) the local velocity shift (default is 0) to refine the radial velocity correction, 3) the number of pixels to be used to calculate the line strength, and a quality flag for the observed line (1=usable, 0=not usable) are included. This input file is read by a python script that uses the information therein 1) to compute the line strength in the observed spectrum as well as in all the 16 synthetic spectra with different abundances in step of 0.1 dex, 2) to compute the line pseudo curve-of-growth from the latter and 3) to finally obtain the chemical abundance by interpolating the observed line strength with that curve.

A.2 Tools for the treatment of observed spectra

This appendix describes some tools used to treat the pipeline-processed CRIFRES+ 1D spectra and obtaining normalised, telluric and radial velocity corrected final spectra (see Sect. 3.1), ready for chemical analysis.

Before performing spectrum normalisation, a sigma clipping procedure is used to clean the spectrum of possible spurious signals from bad pixels and facilitate its normalisation. Pixel signals that deviate more than a selected sigma value are removed by means of the following python line command.

```
clipped_flux=sigma_clip(observed_spectrum,sigma=4,axis=1)
```

A low-pass filtering technique has been used to define the spectrum continuum. In particular, a box smoothing filter with a size of a few hundreds pixels has been applied to each observed spectrum, by means of the following python function.

```
def smooth(flux, box_pts):
    box = np.ones(box_pts)/box_pts
    smooth_flux = np.convolve(flux, box, mode='same')
    return smoothed_flux
```

This function generates a smoothed spectrum representative of the stellar continuum (e.g. red line in Fig. 3.1). The normalised spectrum is obtained by dividing the observed spectrum, cleaned with the sigma clipping, by this smoothed spectrum, via the following python line command.

```
normalized_flux = clipped_flux/smoothed_flux
```

After spectrum normalization, the telluric absorption lines need to be removed. Synthetic telluric spectra from the TAPAS portal (see Sect. 3.1) were used. For all stars, the observation site (e.g. Paranal), the set of molecules present in the atmosphere (e.g. H₂O, O₃, O₂, CO₂, CH₄, N₂O, NO₂), the profile with which the lines have to be convoluted (e.g. Gaussian), the instrumental resolution, the sampling and finally the spectral range (e.g. 19000-24000 Å) need to be selected. For each individual star, the date of observation and celestial coordinates must also be specified in order to derive the airmass. Twelve normalised telluric spectra were generated. Telluric absorption removal has been performed by dividing the observed normalised spectra by the previously obtained synthetic telluric spectra, via the following python line command.

```
tell_corr_flux = normalized_flux/telluric_flux
```

These telluric-corrected spectra (see also Fig. 3.3) are then used to derive the stellar radial velocity. A standard technique to obtain the radial velocity of individual stars is cross-correlation of the observed spectra with suitable templates whose radial velocity is known a priori (see also Sect. 3.2).

The implemented algorithm operates in the following manner. The wavelength axis of the template is shifted using a range of possible Doppler shifts corresponding to the range of radial velocities v_j in steps of 0.1 km s^{-1} that need to be explored. Subsequently, the wavelengths and fluxes of each (one per radial velocity v_j) shifted template are linearly interpolated to match the observed ones and a corresponding cross-correlation value $CC(v_j)$ is computed according to the following formula.

$$CC(v_j) = \sum_{i=1}^N (f_i(\lambda) \times tf_i(\lambda_i - \Delta\lambda_{i,j}))$$

where the sum extends to the N data points in the spectrum, f_i and λ_i are the flux and wavelength of the i -th data point, respectively, tf_i is the corresponding template flux and $\Delta\lambda_{i,j} = \lambda_i(v_j/c)$ is the i -th wavelength Doppler shift.

The best radial velocity is the one that maximize the cross-correlation function.

As shown in Fig. A.4, the peak of the cross-correlation function provides the relative velocity between the observed source and the template. As templates, it is convenient to use synthetic spectra with 0 km s^{-1} radial velocity by construction, spectral resolution and sampling and stellar parameters similar to those of the observed stars, in order to cross-correlate lines of similar depth and width in both the observed and synthetic spectra.

The following python function[†] has been used.

```
rv,cc = pyasl.crosscorrRV(obs_wl,obs_flux,templ_wl,templ_flux,
rvmin=-200,rvmax=200,drv=0.1)
```

An heliocentric correction has been then applied to the inferred radial velocities to account for the motion of the Earth with respect to the Sun and to the baricenter of the Solar system.

The spectrum corrected for heliocentric radial velocity, sometime also named rest-frame spectrum, is obtained by applying the Doppler shift at each wavelength according to the following formula.

```
rest_wavelength = wavelength * (1 - RV/c)
```

where RV is the heliocentric radial velocity of the star.

[†]<https://pyastronomy.readthedocs.io/en/latest/pyaslDoc/aslDoc/crosscorr.html>

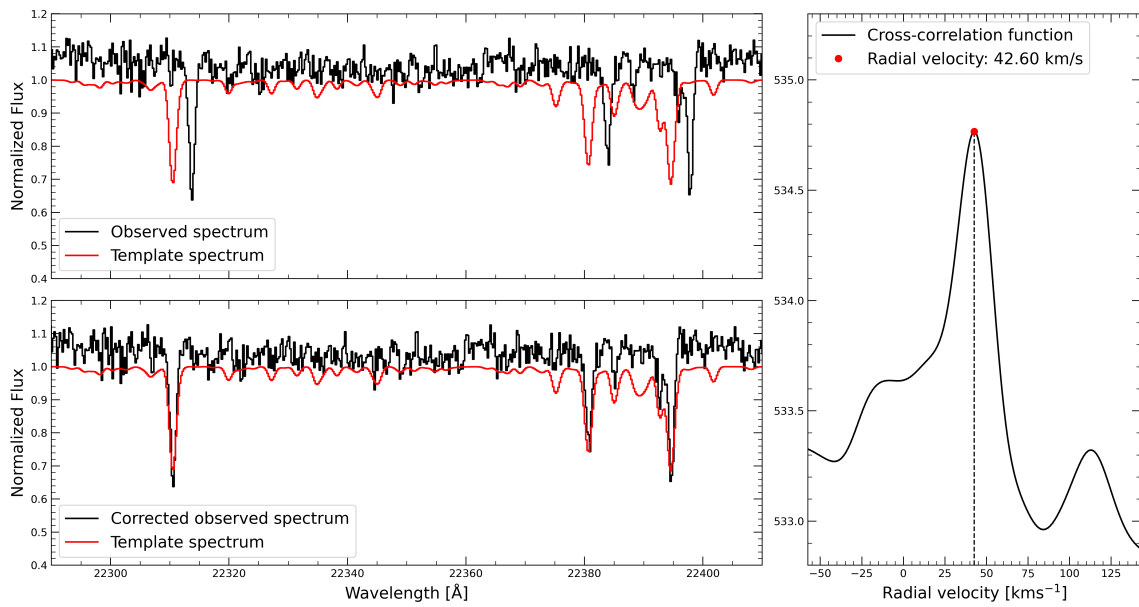


Figure A.4: Example of radial velocity measurement and subsequent correction of the observed spectrum using the cross-correlation technique. Left panels: observed spectrum (black) and template spectrum (red) before (top) and after (bottom) correction for radial velocity. Right panel: the computed cross-correlation function.

A.3 Tools to test spectral synthesis

As discussed in Sect. 3.5, the chemical analysis has been performed by means of spectral synthesis around each line of interest, by using as a figure of merit its strength (see Sec.A.1).

In order to check the effectiveness of such an approach to get reliable abundances from the CRIRES+ spectra, we simulated observed spectra with known stellar parameters and chemical abundances, and we performed the same chemical analysis as in the case of the CRIRES+ spectra.

In particular, such simulated spectra have been obtained by computing synthetic spectra with stellar parameters and chemical abundances as for the real stars, and at the same equivalent resolution $R_{eq}=25,000$ and spectral sampling of the CRIRES+ observed spectra. Then we added a Gaussian noise of 2% to these spectra, consistent with the measured signal-to-noise ratios (typically about 50).

As an example, Table A.1 listed the adopted stellar parameters for two simulated stars, representative of the Liller 1 metal-poor and metal-rich sub-populations, and Fig. A.5 shows the corresponding simulated K-band spectra in the 21000-21500 Å range.

Table A.1: Adopted stellar parameters for two simulated stars, representative of the Liller 1 sub-populations.

Parameter	Star metal poor	Star metal rich
T_{eff}	3480	3600
$\log(g)$	0.30	0.90
ξ	2.00	2.00
[Fe/H]	-0.40	+0.30
$[\alpha/Fe]$	+0.30	+0.00
SNR	50	50

The results of the chemical analysis of these two simulated stars, using the same reference lines and procedures as for the stars observed with CRIRES+, are shown in Fig. A.6.

Differences between the derived abundances and the nominal ones are fully consistent within the errors of a few hundredths dex, that are also the typical errors on the derived abundances of the real stars.

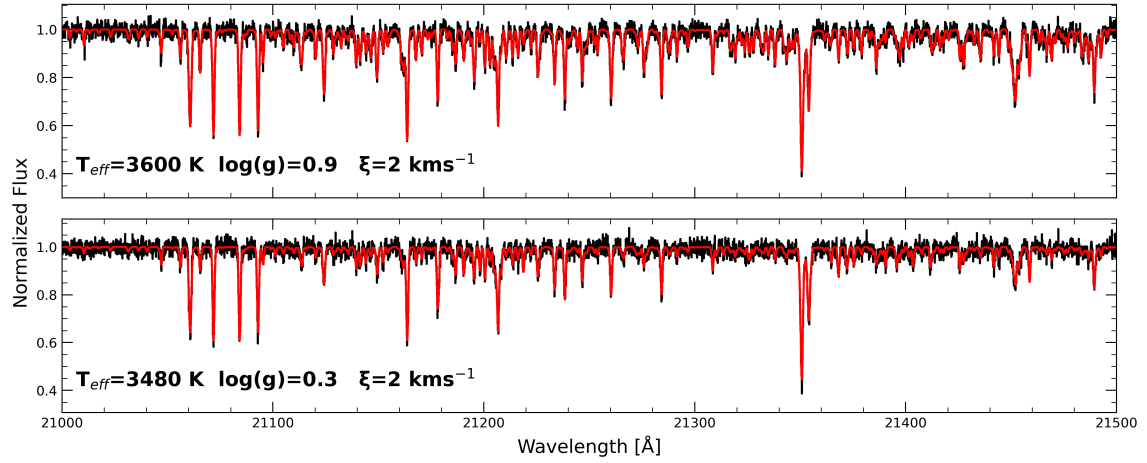


Figure A.5: 2% noisy (black) and noise-free (red) simulated spectra of two stars, representative of the Liller 1 sub-populations (see also Table A.1), in the 21000-21500 Å range.

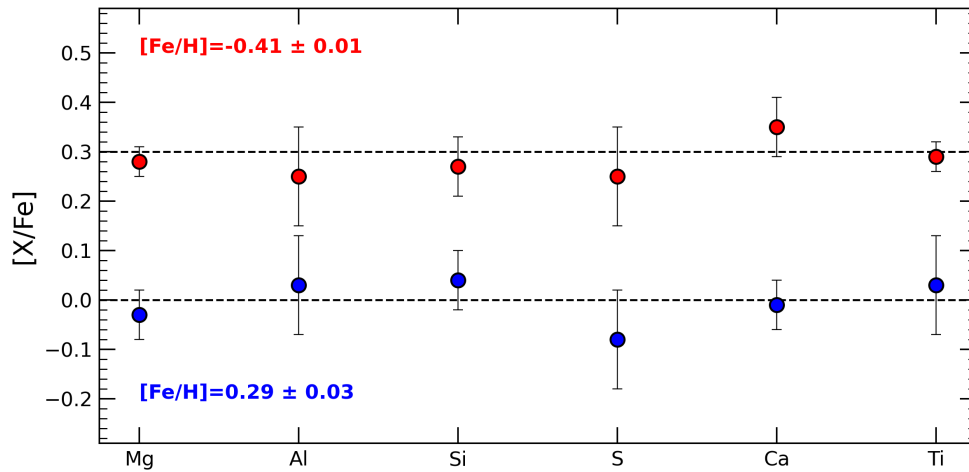


Figure A.6: Obtained abundances of the two test stars. In blue the metal rich star, in red the metal poor one. The dashed lines represent the expected abundances.

Bibliography

- Melike Afşar, Christopher Sneden, Michael P. Wood, James E. Lawler, Zeynep Bozkurt, Gamze Böcek Topcu, Gregory N. Mace, Hwi Hyun Kim, and Daniel T. Jaffe. Chemical Compositions of Evolved Stars from Near-infrared IGRINS High-resolution Spectra. I. Abundances in Three Red Horizontal Branch Stars. *ApJ*, 865(1):44, September 2018. doi: 10.3847/1538-4357/aada0c.
- R. Alvarez and B. Plez. Near-infrared narrow-band photometry of M-giant and Mira stars: models meet observations. *A&A*, 330:1109–1119, February 1998. doi: 10.48550/arXiv.astro-ph/9710157.
- H. Baumgardt, M. Hilker, A. Sollima, and A. Bellini. Mean proper motions, space orbits, and velocity dispersion profiles of Galactic globular clusters derived from Gaia DR2 data. *MNRAS*, 482(4):5138–5155, February 2019. doi: 10.1093/mnras/sty2997.
- Frédéric Bournaud. Bulge Growth Through Disc Instabilities in High-Redshift Galaxies. In Eija Laurikainen, Reynier Peletier, and Dimitri Gadotti, editors, *Galactic Bulges*, volume 418 of *Astrophysics and Space Science Library*, page 355, January 2016. doi: 10.1007/978-3-319-19378-6_13.
- Frédéric Bournaud and Bruce G. Elmegreen. Unstable Disks at High Redshift: Evidence for Smooth Accretion in Galaxy Formation. *ApJ*, 694(2):L158–L161, April 2009. doi: 10.1088/0004-637X/694/2/L158.
- Alessandro Bressan, Paola Marigo, Léo. Girardi, Bernardo Salasnich, Claudia Dal Cero, Stefano Rubele, and Ambra Nanni. PARSEC: stellar tracks and isochrones with the PAdova and TRieste Stellar Evolution Code. *MNRAS*, 427(1):127–145, November 2012. doi: 10.1111/j.1365-2966.2012.21948.x.
- Chiara Crociati, Elena Valenti, Francesco R. Ferraro, Cristina Pallanca, Barbara Lanzoni, Mario Cadelano, Cristiano Fanelli, Livia Origlia, Silvia Leanza, Emanuele Dalessandro, Alessio Mucciarelli, and R. Michael Rich. First Evidence of Multi-iron Subpopulations in the Bulge Fossil Fragment Candidate Liller 1. *ApJ*, 951(1):17, July 2023. doi: 10.3847/1538-4357/acd382.
- Emanuele Dalessandro, Chiara Crociati, Michele Cignoni, Francesco R. Ferraro, Barbara Lanzoni, Livia Origlia, Cristina Pallanca, R. Michael Rich, Sara Saracino, and Elena Valenti. Clues to the Formation of Liller 1 from Modeling Its Complex Star Formation History. *ApJ*, 940(2):170, December 2022. doi: 10.3847/1538-4357/ac9907.
- Bruce G. Elmegreen, Frédéric Bournaud, and Debra Meloy Elmegreen. Bulge Formation by the Coalescence of Giant Clumps in Primordial Disk Galaxies. *ApJ*, 688(1):67–77, November 2008. doi: 10.1086/592190.

- Bruce G. Elmegreen, Debra Meloy Elmegreen, Maria Ximena Fernandez, and Jenna Jo Lemonias. Bulge and Clump Evolution in Hubble Ultra Deep Field Clump Clusters, Chains and Spiral Galaxies. *ApJ*, 692(1):12–31, February 2009. doi: 10.1088/0004-637X/692/1/12.
- C. Fanelli, L. Origlia, E. Oliva, A. Mucciarelli, N. Sanna, E. Dalessandro, and D. Romano. Stellar population astrophysics (SPA) with the TNG. The Arcturus Lab. *A&A*, 645:A19, January 2021. doi: 10.1051/0004-6361/202039397.
- C. Fanelli, L. Origlia, E. Oliva, E. Dalessandro, A. Mucciarelli, and N. Sanna. Stellar population astrophysics (SPA) with the TNG. The chemical content of the red supergiant population in the Perseus complex. *A&A*, 660:A7, April 2022. doi: 10.1051/0004-6361/202142492.
- F. R. Ferraro, E. Dalessandro, A. Mucciarelli, G. Beccari, R. M. Rich, L. Origlia, B. Lanzoni, R. T. Rood, E. Valenti, M. Bellazzini, S. M. Ransom, and G. Cocozza. The cluster Terzan 5 as a remnant of a primordial building block of the Galactic bulge. *Nature*, 462(7272):483–486, November 2009. doi: 10.1038/nature08581.
- F. R. Ferraro, D. Massari, E. Dalessandro, B. Lanzoni, L. Origlia, R. M. Rich, and A. Mucciarelli. The Age of the Young Bulge-like Population in the Stellar System Terzan 5: Linking the Galactic Bulge to the High-z Universe. *ApJ*, 828(2):75, September 2016. doi: 10.3847/0004-637X/828/2/75.
- F. R. Ferraro, C. Pallanca, B. Lanzoni, C. Crociati, E. Dalessandro, L. Origlia, R. M. Rich, S. Saracino, A. Mucciarelli, E. Valenti, D. Geisler, F. Mauro, S. Villanova, C. Moni Bidin, and G. Beccari. A new class of fossil fragments from the hierarchical assembly of the Galactic bulge. *Nature Astronomy*, 5:311–318, January 2021. doi: 10.1038/s41550-020-01267-y.
- R. Genzel, S. Newman, T. Jones, N. M. Förster Schreiber, K. Shapiro, S. Genel, S. J. Lilly, A. Renzini, L. J. Tacconi, N. Bouché, A. Burkert, G. Cresci, P. Buschkamp, C. M. Carollo, D. Ceverino, R. Davies, A. Dekel, F. Eisenhauer, E. Hicks, J. Kurk, D. Lutz, C. Mancini, T. Naab, Y. Peng, A. Sternberg, D. Vergani, and G. Zamorani. The Sins Survey of $z \sim 2$ Galaxy Kinematics: Properties of the Giant Star-forming Clumps. *ApJ*, 733(2):101, June 2011. doi: 10.1088/0004-637X/733/2/101.
- B. Gustafsson, B. Edvardsson, K. Eriksson, U. G. Jørgensen, Å. Nordlund, and B. Plez. A grid of MARCS model atmospheres for late-type stars. I. Methods and general properties. *A&A*, 486(3):951–970, August 2008. doi: 10.1051/0004-6361:200809724.
- A. Immeli, M. Samland, O. Gerhard, and P. Westera. Gas physics, disk fragmentation, and bulge formation in young galaxies. *A&A*, 413:547–561, January 2004. doi: 10.1051/0004-6361:20034282.

- Christian I. Johnson, R. Michael Rich, Chiaki Kobayashi, Andrea Kunder, and Andreas Koch. Light, Alpha, and Fe-peak Element Abundances in the Galactic Bulge. *AJ*, 148 (4):67, October 2014. doi: 10.1088/0004-6256/148/4/67.
- B. Lanzoni, F. R. Ferraro, E. Dalessandro, A. Mucciarelli, G. Beccari, P. Miocchi, M. Bellazzini, R. M. Rich, L. Origlia, E. Valenti, R. T. Rood, and S. M. Ransom. New Density Profile and Structural Parameters of the Complex Stellar System Terzan 5. *ApJ*, 717 (2):653–657, July 2010. doi: 10.1088/0004-637X/717/2/653.
- Dongwook Lim, Andreas J. Koch-Hansen, Sang-Hyun Chun, Seungsoo Hong, and Young-Wook Lee. High-resolution near-infrared spectroscopy of globular cluster and field stars toward the Galactic bulge. *A&A*, 666:A62, October 2022. doi: 10.1051/0004-6361/202243877.
- Alexandra C. Lockwood, John A. Johnson, Chad F. Bender, John S. Carr, Travis Barman, Alexander J. W. Richert, and Geoffrey A. Blake. Near-IR Direct Detection of Water Vapor in Tau Boötis b. *ApJ*, 783(2):L29, March 2014. doi: 10.1088/2041-8205/783/2/L29.
- Ekaterina Magg, Maria Bergemann, Aldo Serenelli, Manuel Bautista, Bertrand Plez, Ulrike Heiter, Jeffrey M. Gerber, Hans-Günter Ludwig, Sarbani Basu, Jason W. Ferguson, Helena Carvajal Gallego, Sébastien Gamrath, Patrick Palmeri, and Pascal Quinet. Observational constraints on the origin of the elements. IV. Standard composition of the Sun. *A&A*, 661:A140, May 2022. doi: 10.1051/0004-6361/202142971.
- D. Massari, A. Mucciarelli, F. R. Ferraro, L. Origlia, R. M. Rich, B. Lanzoni, E. Dalessandro, E. Valenti, R. Ibata, L. Lovisi, M. Bellazzini, and D. Reitzel. Ceci N’est Pas a Globular Cluster: The Metallicity Distribution of the Stellar System Terzan 5. *ApJ*, 795(1):22, November 2014. doi: 10.1088/0004-637X/795/1/22.
- D. Massari, E. Dalessandro, F. R. Ferraro, P. Miocchi, A. Bellini, L. Origlia, B. Lanzoni, R. M. Rich, and A. Mucciarelli. Proper Motions in Terzan 5: Membership of the Multi-iron Subpopulations and First Constraint on the Orbit. *ApJ*, 810(1):69, September 2015. doi: 10.1088/0004-637X/810/1/69.
- D. Massari, H. H. Koppelman, and A. Helmi. Origin of the system of globular clusters in the Milky Way. *A&A*, 630:L4, October 2019. doi: 10.1051/0004-6361/201936135.
- Davide Massari, Alessio Mucciarelli, Emanuele Dalessandro, Francesco R. Ferraro, Livia Origlia, Barbara Lanzoni, Giacomo Beccari, R. Michael Rich, Elena Valenti, and Scott M. Ransom. High-resolution Reddening Map in the Direction of the Stellar System Terzan 5. *ApJ*, 755(2):L32, August 2012. doi: 10.1088/2041-8205/755/2/L32.
- L. Origlia, R. M. Rich, F. R. Ferraro, B. Lanzoni, M. Bellazzini, E. Dalessandro, A. Mucciarelli, E. Valenti, and G. Beccari. Spectroscopy Unveils the Complex Nature of Terzan

5. *ApJ*, 726(2):L20, January 2011. doi: 10.1088/2041-8205/726/2/L20.
- L. Origlia, D. Massari, R. M. Rich, A. Mucciarelli, F. R. Ferraro, E. Dalessandro, and B. Lanzoni. The Terzan 5 Puzzle: Discovery of a Third, Metal-poor Component. *ApJ*, 779(1):L5, December 2013. doi: 10.1088/2041-8205/779/1/L5.
- Livia Origlia, R. Michael Rich, and Sandra Castro. High-Resolution Infrared Spectra of Bulge Globular Clusters: Liller 1 and NGC 6553. *AJ*, 123(3):1559–1569, March 2002. doi: 10.1086/338897.
- Cristina Pallanca, Francesco R. Ferraro, Barbara Lanzoni, Chiara Crociati, Sara Saracino, Emanuele Dalessandro, Livia Origlia, Michael R. Rich, Elena Valenti, Douglas Geisler, Francesco Mauro, Sandro Villanova, Christian Moni Bidin, and Giacomo Becari. High-resolution Extinction Map in the Direction of the Strongly Obscured Bulge Fossil Fragment Liller 1. *ApJ*, 917(2):92, August 2021. doi: 10.3847/1538-4357/ac0889.
- B. Plez. Turbospectrum: Code for spectral synthesis. Astrophysics Source Code Library, record ascl:1205.004, May 2012.
- R. M. Rich, L. Origlia, and E. Valenti. Detailed Abundances for M Giants in Two Inner Bulge Fields from Infrared Spectroscopy. *ApJ*, 746(1):59, February 2012. doi: 10.1088/0004-637X/746/1/59.
- Donatella Romano, Francesco R. Ferraro, Livia Origlia, Simon Portegies Zwart, Barbara Lanzoni, Chiara Crociati, Davide Massari, Emanuele Dalessandro, Alessio Mucciarelli, R. Michael Rich, Francesco Calura, and Francesca Matteucci. Modeling the Chemical Enrichment History of the Bulge Fossil Fragment Terzan 5. *ApJ*, 951(2):85, July 2023. doi: 10.3847/1538-4357/acd8ba.
- S. Tacchella, P. Lang, C. M. Carollo, N. M. Förster Schreiber, A. Renzini, A. E. Shapley, S. Wuyts, G. Cresci, R. Genzel, S. J. Lilly, C. Mancini, S. F. Newman, L. J. Tacconi, G. Zamorani, R. I. Davies, J. Kurk, and L. Pozzetti. SINS/zC-SINF Survey of $z \sim 2$ Galaxy Kinematics: Rest-frame Morphology, Structure, and Colors from Near-infrared Hubble Space Telescope Imaging. *ApJ*, 802(2):101, April 2015. doi: 10.1088/0004-637X/802/2/101.